



HAL
open science

Challenging and Improving the Simulation of Mid-Level Mixed-Phase Clouds Over the High-Latitude Southern Ocean

É. Vignon, S. P Alexander, P. J Demott, G. Sotiropoulou, F. Gerber, T. C J Hill, R. Marchand, A. Nenes, A. Berne

► **To cite this version:**

É. Vignon, S. P Alexander, P. J Demott, G. Sotiropoulou, F. Gerber, et al.. Challenging and Improving the Simulation of Mid-Level Mixed-Phase Clouds Over the High-Latitude Southern Ocean. *Journal of Geophysical Research: Atmospheres*, 2021, 126 (7), pp.e2020JD033490. 10.1029/2020JD033490 . hal-03280181

HAL Id: hal-03280181

<https://hal.sorbonne-universite.fr/hal-03280181v1>

Submitted on 7 Jul 2021

HAL is a multi-disciplinary open access archive for the deposit and dissemination of scientific research documents, whether they are published or not. The documents may come from teaching and research institutions in France or abroad, or from public or private research centers.

L'archive ouverte pluridisciplinaire **HAL**, est destinée au dépôt et à la diffusion de documents scientifiques de niveau recherche, publiés ou non, émanant des établissements d'enseignement et de recherche français ou étrangers, des laboratoires publics ou privés.

Challenging and improving the simulation of mid-level mixed-phase clouds over the high-latitude Southern Ocean

É. Vignon^{1,2}, S. P. Alexander^{3,4}, P. J. DeMott⁵,
G. Sotiropoulou^{6,7}, F. Gerber^{8,9}, T. C. J. Hill⁵, R. Marchand¹⁰,
A. Nenes^{6,11} and A. Berne¹

¹Environmental Remote Sensing Laboratory (LTE), École Polytechnique Fédérale de Lausanne (EPFL),
Lausanne, Switzerland

²Laboratoire de Météorologie Dynamique/IPSL/Sorbone Université/CNRS, UMR 8539, Paris, France

³Australian Antarctic Division, Kingston, Tasmania, Australia

⁴Australian Antarctic Program Partnership, Institute for Marine and Antarctic Science, University of
Tasmania, Hobart, Australia

⁵Department of Atmospheric Science, Colorado State University, Fort Collins

⁶Laboratory of Atmospheric Processes and their Impacts (LAPI), Ecole Polytechnique Fédérale de
Lausanne (EPFL), Lausanne, Switzerland

⁷Department of Meteorology and Bolin Center for Climate Research, Stockholm University, Stockholm,
Sweden

⁸Laboratory of Cryospheric Sciences, School of Architecture, Civil and Environmental Engineering, École
Polytechnique Fédérale de Lausanne (EPFL), Lausanne, Switzerland

⁹WSL Institute for Snow and Avalanche Research SLF, Davos, Switzerland

¹⁰Department of Atmospheric Sciences, University of Washington, Seattle, WA, USA

¹¹ICE-HT, Foundation for Research and Technology Hellas (FORTH), Patras, Greece

Key Points:

- WRF-observation comparison during MARCUS shows the inability of the model in standard configurations to simulate austral mixed-phase clouds;
- A parameterization of ice nucleation based on new INP measurements improves the simulation of supercooled liquid water near cloud top;
- Further parameterization developments targeting the convection at cloud top are needed to reproduce the turbulence-microphysics interplay.

Corresponding author: Étienne Vignon, etienne.vignon@lmd.ipsl.fr

Abstract

Climate models exhibit major radiative biases over the Southern Ocean owing to a poor representation of mixed-phase clouds. This study uses the remote-sensing dataset from the Measurements of Aerosols, Radiation and Clouds over the Southern Ocean (MARCUS) campaign to assess the ability of the Weather Research and Forecasting (WRF) model to reproduce frontal clouds off Antarctica. It focuses on the modeling of thin mid-level supercooled liquid water layers which precipitate ice. The standard version of WRF produces almost fully glaciated clouds and cannot reproduce cloud top turbulence. Our work demonstrates the importance of adapting the ice nucleation parameterization to the pristine austral atmosphere to reproduce the supercooled liquid layers. Once simulated, droplets significantly impact the cloud radiative effect by increasing downwelling longwave fluxes and decreasing downwelling shortwave fluxes at the surface. The net radiative effect is a warming of snow and ice covered surfaces and a cooling of the ocean. Despite improvements in our simulations, the local circulation related to cloud-top radiative cooling is not properly reproduced, advocating for the need to develop a parameterization for top-down convection to capture the turbulence-microphysics interplay at cloud top.

Plain Language Summary

Among the major shortcomings of climate models is a poor representation of clouds over the Southern Ocean. Thanks to new measurements from the Measurements of Aerosols, Radiation and Clouds over the Southern Ocean campaign that took place aboard the Aurora Australis ice breaker, we can now better assess the ability of models to represent clouds off Antarctica. In particular, we focus here on clouds that are mostly composed of ice crystals but that are topped by a thin layer of so-called ‘supercooled’ liquid droplets that form at temperatures below zero Celsius. While the standard version of the model produces clouds composed only of ice, we show that by adapting the formulation of ice crystal formation to the very pristine atmospheric conditions peculiar to the Southern Ocean it is possible to successfully reproduce thin layers of supercooled liquid droplets observed in mixed-phase clouds. The latter significantly changes how much sunlight these clouds reflect to space, which is critical to understanding the climate. Compared to ice crystals, liquid droplets tend to reflect more solar energy towards space and

61 at the same time, they enhance the cloud infrared emission towards the surface of the
62 Antarctic ice sheet.

63 **1 Introduction**

64 The Southern Ocean is a region where radiative biases in models involved in the
65 5th Coupled Model Intercomparison Project (CMIP) are amongst the largest globally
66 (Flato & coauthors, 2013; Hyder et al., 2018). Such biases have been attributed to a poor
67 representation of clouds that cover more than 80 % of the total Southern Ocean surface
68 on average (Mace, 2010) and that are mostly of mixed-phase composition, i.e. contain-
69 ing both ice crystals and supercooled liquid water (SLW). Low-level mixed-phase clouds
70 are the primary source of those biases (Bodas-Salcedo et al., 2014) but mid-level clouds
71 associated with the passage of warm fronts are also partly responsible (Mason et al., 2014).
72 While the climate sensitivity in some of recent climate models highly depends on South-
73 ern Ocean clouds (Gettelman et al., 2019; Zelinka et al., 2020), substantial shortcom-
74 ings regarding the simulation of mixed-phase clouds persist (e.g., Lenaerts, Van Tricht,
75 Lhermitte, & L'Ecuyer, 2017; Kawai et al., 2019).

76 The SLW amount in austral mixed-phase clouds is particularly high in summer,
77 at low altitude and over ice-free surfaces (Listowski et al., 2019). Highly reflective SLW
78 droplets substantially enhance the cloud albedo and therefore the amount of shortwave
79 radiation reflected towards space (Kay et al., 2016; Protat et al., 2017). By significantly
80 increasing the cloud optical depth, the amount of SLW in clouds is also critical for their
81 radiative forcing in the infrared spectrum.

82 Atmospheric models generally struggle to reproduce the albedo (Bodas-Salcedo et
83 al., 2014, 2016; Varma et al., 2020) and the surface longwave radiative flux associated
84 with frontal clouds over the Southern Ocean, that can be further advected over the Antarc-
85 tic ice sheet (King et al., 2015; Listowski & Lachlan-Cope, 2017; Vignon et al., 2018; Hines
86 et al., 2019; Ricaud et al., 2020). This is highly problematic for reproducing the net cloud
87 radiative forcing at the ice sheet surface and for predicting melting events associated with
88 oceanic intrusions of warm, moist and cloudy air masses (Nicolas et al., 2017; Wille et
89 al., 2019; Silber, Verlinde, Cadeddu, et al., 2019; Gilbert et al., 2020). Along the Antarc-
90 tic edge, SLW is also a key ingredient for cloud (Zhang et al., 2019; Silber, Fridlind, et
91 al., 2019; Lubin et al., 2020) and precipitation formation and growth, in particular through

92 secondary ice production processes (Young et al., 2019; Sotiropoulou et al., 2020) and
93 the riming of snowflakes (Grazioli et al., 2017; Vignon, Besic, et al., 2019).

94 In mixed-phase clouds, SLW is thermodynamically unstable and depletes through
95 transfer of water vapor towards ice crystals by the Wegener-Bergeron-Findeisen (WBF)
96 process. The presence of SLW in mixed-phase clouds for more than a few hours is thus
97 explained by a complex interplay between radiative exchanges, turbulent mixing and mi-
98 crophysics (Morrison et al., 2012; A. V. Korolev & Mazin, 2003). A body of literature
99 has documented this *a priori* surprising resilience of SLW in cold clouds, especially in
100 boundary-layer clouds in the Arctic (see reviews in A. Korolev et al., 2017 and Andronache
101 & coauthors, 2017). In particular, for typical mixed-phase stratocumulus and altocumu-
102 lus found at mid- or high latitudes (Hogan et al., 2003; P. A. Barrett et al., 2020), the
103 SLW resilience results from the following mechanism. At cloud top, the radiative cool-
104 ing of the air - and to a second extent the sublimation and evaporation of hydromete-
105 ors - drive a top down turbulent mixing that in turn generates compensating updrafts.
106 If the updrafts are intense enough (A. V. Korolev & Mazin, 2003), the relative humid-
107 ity can exceed saturation with respect to liquid through air adiabatic cooling during as-
108 cent. Cloud droplets thus form and are advected upward, thereby forming a thin - a few
109 hundred meter deep - layer of SLW at cloud top, below which ice crystals grow through
110 the WBF process and possibly other mechanisms like riming and then sediment. SLW
111 formation is further favored in conditions of high concentrations of cloud condensation
112 nuclei (CCN) and low concentrations of ice nucleating particles (INPs).

113 The difficulty for atmospheric models to simulate SLW in austral mixed-phase clouds
114 - be they either low-level stratocumulus or mid-level clouds - mostly lies in: *i*) their too
115 coarse vertical resolution since SLW layers are a few tens or hundreds meters deep, i.e.,
116 often thinner than model layers in common atmospheric models (A. I. Barrett et al., 2017b);
117 *ii*) in a deficient representation of the turbulent mixing at the sharp cloud top bound-
118 ary (Sotiropoulou et al., 2016) and *iii*) inadequate parameterizations or tuning of cold
119 microphysical processes for the typical conditions encountered at high latitude (Forbes
120 & Ahlgrim, 2014; A. I. Barrett et al., 2017a; Furtado et al., 2016; Listowski & Lachlan-
121 Cope, 2017). The atmosphere above the Southern Ocean being particularly pristine, with
122 INPs in the boundary layer that mostly originate from sea spray aerosols only (DeMott
123 et al., 2016; McCluskey et al., 2018; Uetake et al., 2020), many current model formula-
124 tions for ice nucleation may be inadequate. Such formulations were indeed mostly de-

125 veloped for mid-latitude conditions where much higher concentrations of INPs are typ-
126 ically present. They can potentially lead to substantial underestimation of SLW droplets
127 in clouds and hence major radiative biases in models (Vergara-Temprado et al., 2018).
128 In addition, previously underappreciated processes like secondary ice production through
129 ice particle break-up also seem particularly critical to explain the concentration of ice
130 crystals in clouds over the Antarctic coast (Young et al., 2019; Sotiropoulou et al., 2020).

131 During the austral summer 2017-2018, the Measurement of Aerosols, Radiation and
132 Clouds over the Southern Ocean (MARCUS) campaign was conducted aboard the Aus-
133 tralian ice-breaker Aurora Australis as the ship made three return crossings of the South-
134 ern Ocean from Hobart to East Antarctica in order to resupply the three Australian Antarc-
135 tic stations (Sato et al., 2018; Alexander et al., 2020).

136 The MARCUS campaign offers a unique dataset to evaluate the ability of atmo-
137 spheric models to represent frontal mixed-phase clouds adjacent to the Antarctic coast
138 and to foster the development, evaluation and tuning of adequate microphysics and tur-
139 bulence parameterizations in models.

140 In this study, we make use of those data to evaluate and improve the representa-
141 tion of austral mixed-phase clouds in the Weather Research and Forecasting (WRF) model.
142 We focus on clouds associated with the passage of a warm front between the 14 and the
143 16 February 2018 above Mawson station (67.6°S, 62.9°E, identified with a green dot in
144 the map plotted in Figure 1). This case study corresponds to the third precipitation event
145 described in Alexander et al. (2020). We pay particular attention to the challenging rep-
146 resentation of SLW layers at the top of mid-altitude clouds preceding and following the
147 front. Beyond the WRF evaluation, the aim of the paper is to identify priorities and pro-
148 pose pathways for parameterization development and tuning which can assist cloud mod-
149 eling over the Southern Ocean.

150 **2 Meteorological setting, observations and simulations**

151 **2.1 Remotely-sensed and in situ observations from the Aurora Australis**

152 A comprehensive suite of instrumentation from the second Atmospheric Radiation
153 Measurement (ARM) Mobile Facility (McFarquhar et al. 2020, submitted to BAMS) was
154 deployed aboard the ship. A vertically-pointing W-band (95 GHz) Doppler cloud radar
155 (MWACR) sampling every 2 s and set-up on a stabilizing platform provided vertical pro-

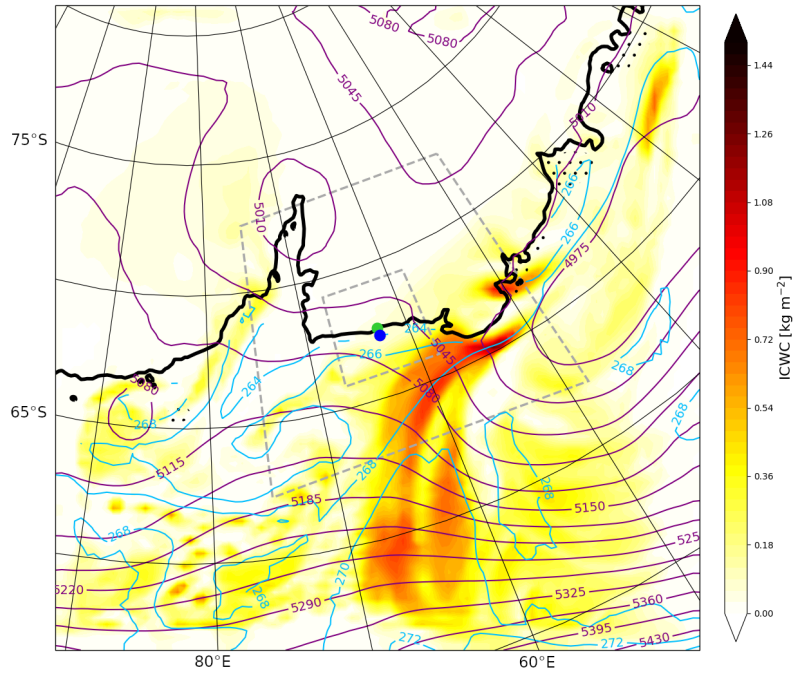


Figure 1. Map of synoptic conditions around Mawson station at 00 UTC, 15 February 2018, from the ctrl Polar WRF simulation (27-km resolution domain). The purple (resp. cyan) contours show the 500 hPa geopotential height in m (resp. the 900 hPa temperature above the Ocean in K). The color shading shows the vertically integrated condensed water content (ICWC, sum of cloud liquid droplets, cloud ice crystals, snow, rain and graupel species). Dashed grey lines delimit the 9-km and 3-km resolution domains. Regions where the sea ice concentration is greater than 0.5 are marked with small black dots. The green circle locates Mawson station while the blue circle indicates the position of the Aurora Australis at 00 UTC, 15 February 2018.

156 files of reflectivity, Doppler velocity and spectral width. The reflectivity measurements
157 were calibrated following Kollias et al. (2019). During this case study, the ship was at
158 Mawson station during standard working hours, but moved a few nautical miles to the
159 north during local ‘night’. In any case, the ship was in very calm waters thanks to off-
160 shore ice that damped sea swells. Subsequently, the radar Doppler velocity uncertainty
161 due to ship’s heave is very low (the standard deviation of the heave velocity during the
162 three days of interest is lower than 0.01 m s^{-1}). From the processing of Doppler veloc-
163 ity time series, it is possible to estimate the dissipation rate ϵ of turbulent kinetic en-
164 ergy (TKE) within the cloud (see Sect. 1 of the supporting information). A micro-pulse
165 lidar (MPL) with a polarization sensitive system and a 5-min temporal resolution allowed
166 for the identification of SLW layers following Alexander and Protat (2018). Further de-
167 tails on radar and lidar data processing, uncertainties and analysis are available in Alexander
168 et al. (2020). Radiosondes were launched from the ship every six hours - 0530, 1130, 1730,
169 2330 UTC (Sato et al., 2018) - and standard meteorological variables were also measured,
170 including downward shortwave and longwave radiative fluxes. The liquid water path (LWP)
171 was estimated from microwave radiometer data following Marchand et al. (2003).

172 Ice nucleating particles were also measured from aerosol filter collections, as in prior
173 ship campaigns (McCluskey et al., 2018). Cumulative temperature spectra of the num-
174 ber concentration of INPs active via immersion freezing were derived from data collected
175 on the freezing of dilute (purified) water droplet suspensions of collected aerosols using
176 the Colorado State University ice spectrometer instrument system (McCluskey et al., 2018).
177 Details of the instrument methods, clean protocols, calculation of cumulative INPs per
178 volume of suspension, conversion of these to numbers per liter of sampled air versus tem-
179 perature, and calculation of confidence intervals (95%) are discussed in DeMott et al.
180 (2018). Filter samples were 24 or 48 hour collections, representing approximately 21 or
181 42 m^3 of air, respectively. Temperature spectra (six represented) of the INP concentra-
182 tions measured close to Mawson station during MARCUS are plotted in Figure 2.

183 **2.2 WRF simulations**

184 This work is based on the version 4.1.1 of the WRF model. The simulation con-
185 figuration follows that used by Vignon, Besic, et al. (2019). The model has been run with
186 a downscaling method where a 27-km resolution parent domain contains a 9-km reso-
187 lution domain which itself contains a $102 \times 102 \text{ km}^2$ nest at a 3-km resolution (see Fig-

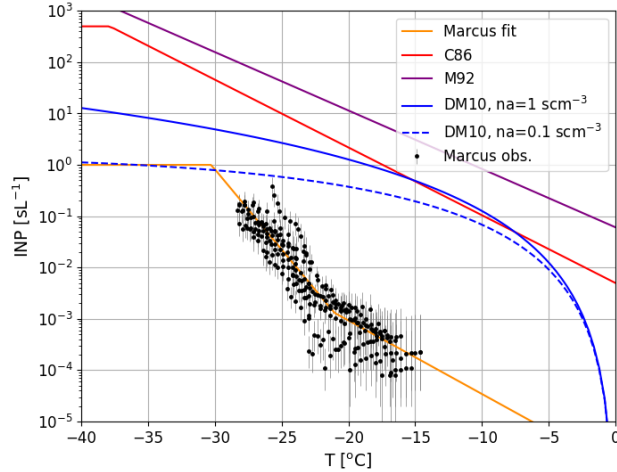


Figure 2. Temperature spectrum of the INP concentration in sL^{-1} (per standard litre). Black dots show measurements off Mawson station during the present MARCUS case study. Errorbars represent the 95% confidence intervals calculated in the same manner as in McCluskey et al. (2018). The orange line shows a fit on the data (see eq. 1). The red line shows the relationship from Cooper (1986) (C86). The purple line shows eq. 2.6 in Meyers et al. (1992) (M92). Blue lines show the DeMott et al. (2010)’s relationship for two extreme values of the concentration of aerosols larger than $0.5 \mu\text{m}$ (n_a) which commonly ranges between 0.1 and 1 scm^{-3}

188 ure 1). Note that achieving a 3-km resolution is needed to correctly capture the dynam-
 189 ics of Antarctic katabatic winds and in particular their coastal transition (Vignon, Traullé,
 190 & Berne, 2019; Vignon et al., 2020). All WRF domains have been built with the same
 191 polar stereographic projection and they are centered over Mawson station. The nesting
 192 is one way i.e. no information is passed in return from one domain to its parent. Lat-
 193 eral forcings, sea ice concentration, sea surface temperature and initial conditions are from
 194 the ERA5 reanalysis (Hersbach et al., 2020). The topography is from the 1-km resolu-
 195 tion Reference Elevation Model of Antarctica dataset (Howat et al., 2019). The model
 196 is run with 96 vertical levels up to 50 hPa. The so-called ‘standard’ grid (black circles
 197 in Figure 3) is automatically generated by WRF after setting the vertical level number.
 198 It shows layer thicknesses between 200 and 250 m in the mid-troposphere. Using 1D sim-
 199 ulations of mixed-phase altocumulus, A. I. Barrett et al. (2017b) stress that a resolution
 200 of at least 100 m is needed to sustain a SLW layer at cloud top. A so-called ‘refined’ grid
 201 has thus been set-up to refine the vertical resolution in the mid-troposphere to about 100
 202 m at the expense of the representation of the stratosphere (grey crosses in Figure 3).

203 Simulations start on February, 14 2018 00 UTC corresponding to a 17 h spin-up
204 time before the arrival of the first frontal clouds above the ship location. To allow for
205 a concomitant comparison between *in situ* observations and simulations and to ensure
206 a realistic synoptic dynamics in the model, the 27-km resolution domain has been nudged
207 above the boundary layer towards ERA5 reanalysis for zonal and meridional wind speed,
208 with a relaxation time scale of 6 h. The nudging only helps provide the best lateral forc-
209 ing for the free 9-km and 3-km resolution domains. The physics options employed through-
210 out the study include the new version of the Rapid Radiative Transfer Model for Gen-
211 eral Circulation Models radiation scheme for longwave and shortwave spectra, the Noah
212 land surface model with adaptations by Hines and Bromwich (2008) and the Mellor-Yamada-
213 Nakanishi-Niino (MYNN) planetary boundary layer scheme coupled with its associated
214 surface layer scheme. For the domains with a resolution greater than or equal to 9 km,
215 the Kain-Fritsch cumulus scheme has been activated. For a proper comparison with MWACR
216 data, W-band radar reflectivity from WRF outputs has been calculated by means of the
217 Cloud Resolving Model Radar Simulator (CR-SIM, Oue et al., 2020) version 3.1. CR-
218 SIM uses the T-matrix method for computing the scattering properties of cloud water,
219 cloud ice, rain, snow, graupel, and hail hydrometeors. In this study, CR-SIM has been
220 configured as a virtual MWACR vertically profiling radar - with a frequency of 94 GHz
221 (close to the 95 GHz frequency of the real instrument) and similar radar beamwidth and
222 range resolution - that follows the track of the Aurora Australis.

223 ***2.2.1 Microphysical scheme setting***

224 We employ the microphysical parameterization from Morrison et al. (2005) which
225 was shown to produce more realistic amounts of liquid water in Antarctic clouds com-
226 pared to less advanced WRF parameterizations and also produces realistic precipitation
227 in coastal Adélie Land (Listowski & Lachlan-Cope, 2017; Hines et al., 2019; Vignon, Besic,
228 et al., 2019). The scheme has a single-moment treatment of cloud droplets and a double-
229 moment treatment of cloud ice, rain drops, snow and graupel particles. The activation
230 of cloud droplets on CCN is not parameterized in the Morrison scheme (except when cou-
231 pling WRF with its chemical module) and the droplet number concentration is a con-
232 stant number. We set it to 100 cm^{-3} , a value that reasonably concurs with other stud-
233 ies over the Antarctic coast and with CCN measurements collected aboard the Aurora
234 Australis during MARCUS (see Sect. 2 of the supporting information).

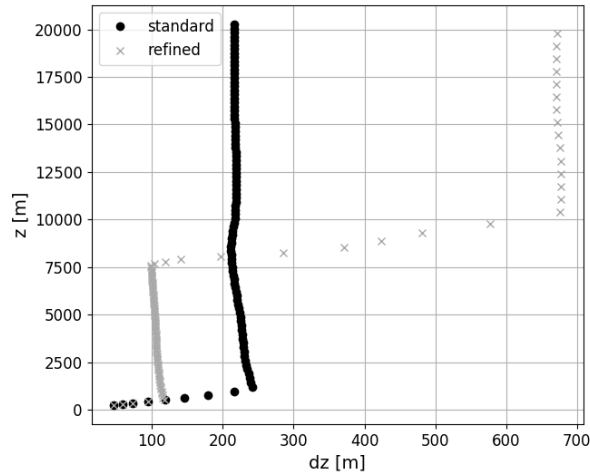


Figure 3. Mean altitude of WRF η levels (z) plotted versus the corresponding layer thickness (dz). Black circles refer to the ‘standard’ 96-level grid. Grey crosses refer to the ‘refined’ 96-level grid with thinner layers in the low- and mid-troposphere.

235 Regarding primary ice production, tendencies of ice number and mass concentra-
 236 tions associated with homogeneous freezing of droplets (at temperatures $\leq -40^\circ\text{C}$) and
 237 three heterogeneous ice nucleation mechanisms are parameterized and are active at tem-
 238 peratures $\leq -4^\circ\text{C}$. In our control simulations, immersion freezing of cloud droplets and
 239 raindrops is taken into account following the stochastic approach of Bigg (1953). Con-
 240 tact freezing is parameterized as a flux of contact INP to cloud droplets and the num-
 241 ber of contact nuclei is given by Meyers et al. (1992) (M92). Deposition/condensation
 242 freezing nucleation is parameterized as a nudging term towards an INP concentration
 243 predicted as a function of temperature following Cooper (1986) (C86). Although our con-
 244 trol (ctrl) simulation has been run with this configuration, the heterogeneous nucleation
 245 schemes are questionable for our study case. First, Bigg (1953)’s scheme based on lab-
 246 oratory data does not explicitly account for ice nuclei and it was shown to be poorly re-
 247 liable for polar conditions (e.g., de Boer, Hashino, Tripoli, & Eloranta, 2013; Paukert &
 248 Hoose, 2014). Second, except at temperatures warmer than about -10°C where contact
 249 freezing dominates, the ice production in the ctrl WRF simulation during MARCUS is
 250 dominated by the deposition/condensation freezing nucleation scheme, but especially at
 251 temperatures lower than -15°C (see Figure S2). Immersion freezing nucleation is thought
 252 to be the dominant nucleation mode in most mixed-phase clouds (Andronache & coau-

253 thors, 2017). It is likely that this mode is represented in the mixed-phase cloud obser-
 254 vations from C86 that are parameterized as deposition/condensation freezing in WRF,
 255 but the number concentrations are representative of the mid-latitude, continental regions
 256 where the observations were primarily collected. Indeed, the INP concentration prescribed
 257 in the C86's deposition nucleation scheme is much higher than the measured INP con-
 258 centration in the immersion freezing mode for the Mawson region at the time of this case
 259 study (Figure 2). This excess of INP also impedes the generation of SLW and of all sub-
 260 sequent freezing processes.

261 As underlined by O'Shea et al. (2017), C86 and M72 parameterizations were de-
 262 veloped for continental conditions in which the INP concentrations are several orders of
 263 magnitude higher than in the pristine atmosphere above the Southern Ocean (DeMott
 264 et al., 2016; Kanji et al., 2017). DeMott et al. (2010) further developed an INP param-
 265 eterization using not only the temperature but also the concentration of aerosols. This
 266 parameterization better predicts the ice crystal number concentration present in clouds
 267 over the Antarctic Peninsula than C86 or M92 (Listowski & Lachlan-Cope, 2017). How-
 268 ever it overestimates the INP concentration off Mawson station (Figure 2) and using it
 269 instead of C86's formulation only - as in Young et al. (2019) - decreases the ice nucle-
 270 ation rate but maintains ice formation at temperatures lower than -20°C (see Figure S2).

271 We thus replaced all the heterogeneous nucleation parameterizations in the Mor-
 272 rison microphysical scheme with a unique empirical one - reflecting immersion freezing
 273 - in the manner of Paukert and Hoose (2014). Note that the Bigg's parameterization is
 274 nonetheless kept active for the freezing of big rain drops. INP measurements during MAR-
 275 CUS have first been fitted with the following equation (see orange line in Figure 2):

$$\log_{10}(N_{INP}) = \begin{cases} -0.14(T - T_1) - 2.88, & \text{if } T > T_1 \\ -0.31(T - T_1) - 2.88, & \text{if } T_2 \leq T \leq T_1 \\ 0.0 & \text{if } T < T_2 \end{cases} \quad (1)$$

276 with N_{INP} the INP number concentration in sL^{-1} , T the temperature in $^{\circ}\text{C}$, $T_1 =$
 277 -21.06°C and $T_2 = -30.35^{\circ}\text{C}$. INP measurements were performed at $T > -28^{\circ}\text{C}$
 278 questioning extrapolation of the curve at very low temperatures. Here, we taper the ex-
 279 ponential increase with decreasing temperature and constrain N_{INP} not to exceed 1 sL^{-1} ,
 280 a value close to the prediction from the DeMott et al. (2010)'s parameterization for

low aerosol concentrations (Figure 2). Setting such a threshold is motivated by recent measurements during the CAPRICORN campaign over the Southern Ocean in McCluskey et al. (2018). The authors revealed that the INP concentration in the immersion mode no longer increases with decreasing temperature - staying below 1 sL^{-1} when temperature is lower than about -28°C . Similar behavior has been observed for other geographical contexts (Kanji et al., 2017).

Then, the ice crystal production term follows the equation:

$$\left. \frac{dN_i}{dt} \right|_{\text{nucleation}} = \begin{cases} \frac{N_{INP} - (N_i + N_s + N_g)}{\Delta t}, & \text{if } N_{INP} > N_i + N_s + N_g \\ 0.0 & \text{otherwise} \end{cases} \quad (2)$$

where Δt the model timestep and N_i , N_s and N_g the number concentration of ice crystals, snowflakes and graupel particles respectively. As this empirical parameterization reflects immersion freezing, the produced mass of cloud ice is removed from cloud liquid water. It is worth noting that this new ice nucleation parameterization is based on INP measurements in the boundary-layer off Mawson station. 5-day back-trajectories revealed that the air parcels arriving in the mid-troposphere above the ship during the study case mostly originate from the north and west of the station and has been lifted from the marine boundary-layer in the vicinity of the station (see Figure S3). The present nucleation scheme should therefore be reasonably valid in both boundary-layer and mid-level frontal clouds.

Furthermore, the Morrison scheme accounts for secondary ice production through the rime-splintering process (Hallett-Mossop) in the $[-8^\circ\text{C}, -3^\circ\text{C}]$ temperature range. However, Young et al. (2019) show that this process should be artificially enhanced by a factor of 10 to reproduce the observed ice crystal concentrations over the Weddell Sea. Sotiropoulou et al. (2020) suggest that it may be due to the absence of parametrization for the secondary ice production through ice particle break-up after hydrometeor collision. By default in our simulations we do not activate a parameterization of collisional break-up but complementary sensitivity experiments have been carried out.

2.2.2 *Cloud top turbulence parameterization*

SLW layers at cloud top are a few tens or hundreds of meters deep (Sedlar et al., 2012; Sotiropoulou et al., 2016), i.e. of comparable width or even thinner than common

308 atmospheric model layers, and they are characterized by a vigorous turbulence that is
 309 critical to generate and maintain the SLW. This turbulence should be represented in mod-
 310 els. However, cloud tops are regions of sharp vertical gradients of atmospheric proper-
 311 ties which are difficult to simulate with the current vertical resolutions of models. The
 312 turbulent mixing at cloud top - or entrainment - has been and is still an active subject
 313 of research especially for warm stratocumulus found over the tropical oceans (e.g., Stevens,
 314 2002; Mellado, 2017). In particular, representing the buoyancy flux and the subsequent
 315 top-down convection associated with cloud top radiative cooling and to a lesser extent,
 316 with the evaporation or sublimation of condensates (see for instance large eddy simu-
 317 lation studies in Brient, Couvreur, Villefranque, Rio, & Honnert, 2019), requires spe-
 318 cific parameterizations (Lenderink & Holtslag, 2000).

319 Some studies using 1-order turbulent mixing schemes proposed to adapt the ver-
 320 tical profiles of the eddy-diffusivity coefficient between the ground and the cloudy boundary-
 321 layer top depending on the radiative and evaporative cooling (Lock et al., 2000; Wilson,
 322 2015; Ghonima et al., 2017). However, such schemes do not properly apply for mid-tropospheric
 323 clouds. In this study, we follow the approach of Guo et al. (2019) based on the pioneer-
 324 ing ideas of Deardoff (1972), Lock (1998) and Grenier and Bretherton (2001). This study
 325 includes a specific parameterization for the TKE production term associated with the
 326 buoyancy flux at the top of a liquid cloud. Briefly, this parameterization accounts for
 327 the buoyancy flux associated with the fraction of the radiative flux divergence that is not
 328 explicitly resolved by the model due to its too coarse vertical resolution. This additional
 329 TKE production term P_R can read:

$$P_R = \mathcal{F}(q_c, p) \frac{g}{\theta_v} \frac{\Delta_z F_{LW} \Delta z}{c_p \rho \Pi} \quad (3)$$

330 where g is the acceleration of gravity, θ_v is the virtual potential temperature, ρ is
 331 the air density, c_p is the air heat capacity, Π is the Exner function, $\Delta_z F_{LW}$ is the long-
 332 wave radiative flux vertical divergence at cloud top and Δz is the cloud top model layer
 333 depth. $\mathcal{F}(q_c, p)$ is a function of the cloud liquid water content q_c and pressure p and is
 334 bounded between 0 and 1. Because estimating \mathcal{F} for a mixed-phase cloud would be much
 335 more complex, we decide to follow a simplified approach:

$$P_R = \phi \frac{g}{\theta_v} \frac{\Delta_z F_{LW} \Delta z}{c_p \rho \Pi} \quad (4)$$

336 with ϕ is tuning coefficient ranging between 0 and 1. By default, we set $\phi = 0.05$
 337 (value that gives reasonable cloud top liquid content and turbulence, see next section)
 338 but the sensitivity to this value will be assessed.

339 **3 Results**

340 **3.1 Brief description of the evolution of clouds and precipitation from** 341 **observations**

342 The synoptic circulation and the cloud properties during our case study are thor-
 343 oughly analysed in Alexander et al. (2020). We provide here a brief description of the
 344 evolution of clouds and precipitation from observations to help the interpretation of model
 345 results. The synoptic meteorological conditions at 00 UTC, 15 February 2018 in the ctrl
 346 WRF simulation are plotted in Figure 1. A synoptic weather system manifesting as a
 347 minimum of 500-hPa geopotential height sets at the north-west of Mawson, advecting
 348 warm and moist oceanic air towards the ice sheet along its eastern flank. In particular,
 349 a zonally elongated tongue of integrated condensed water content (shading) is moving
 350 towards the station and the ship (blue dot). This tongue preceding a warm sector (tem-
 351 perature in cyan contours) corresponds to the warm front of the system. During the 15
 352 and 16 February, the warm front moves to the south-east of the station and dissipates.
 353 The ship thus enters the warm sector, the mid-tropospheric flow above it progressively
 354 changes from a northerly to a westerly direction while the low-level flow, characterized
 355 by a clear katabatic jet at about 500 m a.s.l., keeps an easterly direction (Alexander et
 356 al., 2020). Meanwhile, the cold front of the system remains far from the coast over the
 357 Southern Ocean and the extra-tropical cyclone progressively weakens at the west of Maw-
 358 son and disappears during the second half of the 16 February.

359 Figure 4 shows the time-height plot of the MWACR reflectivity (panel a), Doppler
 360 velocity (panel b) and Doppler spectral width (panel c) above the ship during the event.
 361 Note that the radar ceased functioning between 13 and 17 UTC, 15 February. In panel
 362 a, black contours indicate regions identified as SLW cloud layers using the MPL data.
 363 Panel a indicates a pre-precipitation virga period (16 UTC, 14 February to 02 UTC, 15
 364 February) during the arrival of the warm front above the ship and is characterized by

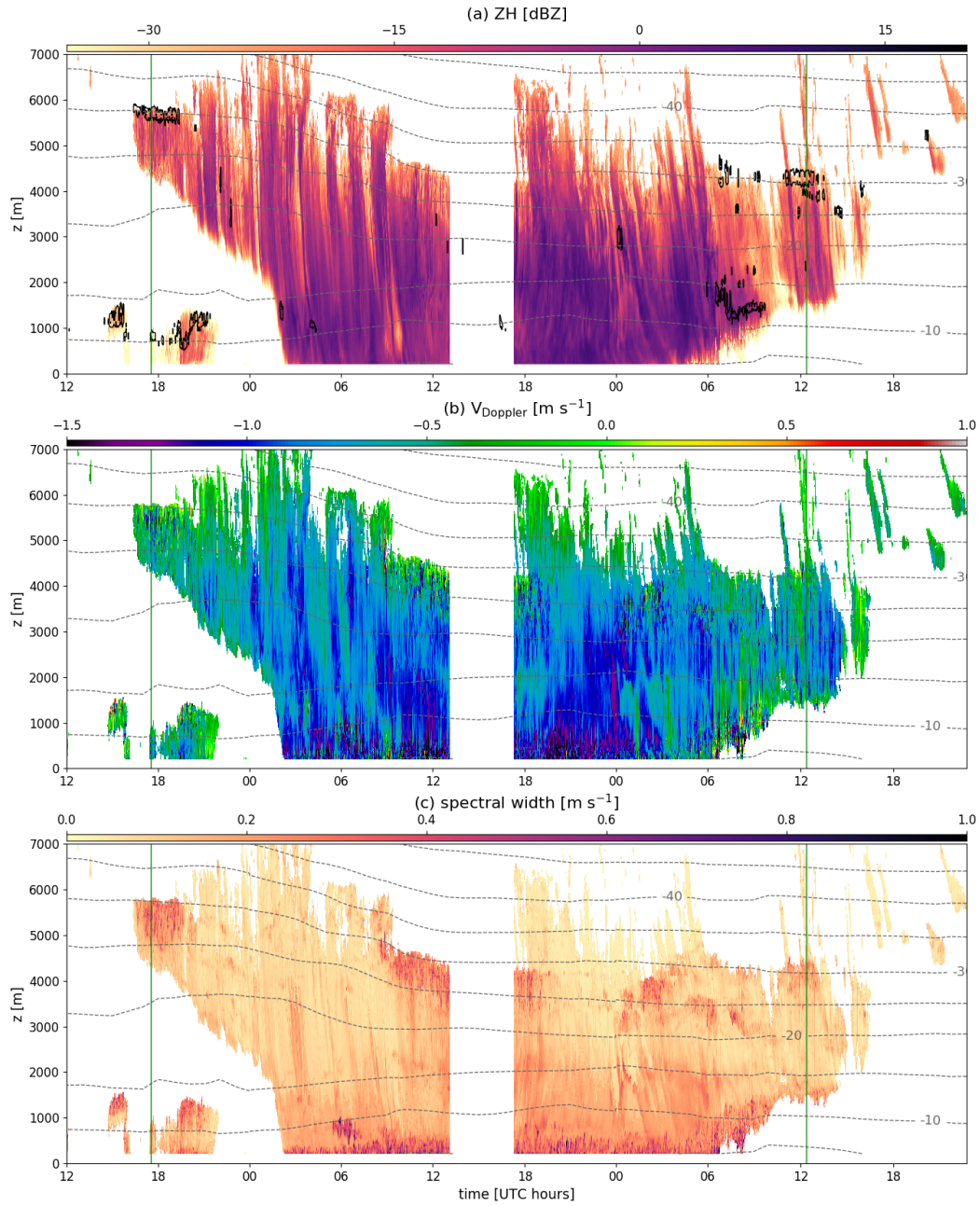


Figure 4. Time height plots of the radar reflectivity ZH (a), Doppler velocity V_{Doppler} (b) and Doppler spectral width (c) measured by the MWACR above the ship between the 14 and 16 February 2018. Grey contours indicate the air temperature (5°C intervals) from the ERA5 reanalyses. Vertical green lines indicate the two specific times analyzed in Figure 6. In panel a, black outlines locate regions where the MPL detects SLW.

365 significant reflectivity values in altitude but not at the surface. This period is followed
 366 by actual surface precipitation within the warm sector - with high reflectivity values at
 367 the first radar gate - which is followed by a post-precipitation phase (06 to 17 UTC, 16
 368 February) when the extra-tropical cyclone dissipates. Such temporal structure (pre-precipitation
 369 virga, surface precipitation, post-precipitation virga) associated with the passage of a
 370 warm front above the station was shown to be representative of the precipitation events
 371 affecting the coast of Adélie Land (Jullien et al., 2020), East Antarctica. From the li-
 372 dar data, clear SLW layers are particularly identified:

- 373 1. at the top of boundary-layer stratocumulus upstream of the warm front in the cool
 374 sector, within the first 1500 m a.s.l. and between 15 and 22 UTC, 14 February;
- 375 2. at the top of the first high frontal clouds (altocumulus), just above pre-precipitation
 376 iced-virga between 17 and 21 UTC, 14 February;
- 377 3. at the top of the boundary-layer (about 1500 m a.s.l.) between 6 and 10 UTC, 16
 378 February;
- 379 4. sitting on top of post-precipitation ice virga at about 4500 m a.s.l. between 11 and
 380 13 UTC, 16 February;

381 Their depth is generally comprised between 100 and 350 m, although we note this is likely
 382 underestimating the full vertical extent of some of these SLW layers due to full lidar sig-
 383 nal attenuation (see Figure S4). The Doppler velocity field shows that where SLW is present,
 384 weakly-negative or even positive values of the mean vertical velocity are measured (see
 385 Figure 4b and the Doppler velocity distribution conditioned to SLW patches in Figure
 386 S1b). Below SLW layers, one can point out rapid alternations of strongly and weakly neg-
 387 ative Doppler velocities. Similarly, the Doppler spectral width - that strongly depends
 388 on turbulence - exhibits large values within and in the few hundred meters below SLW
 389 layers (Figure 4c). The creation and resilience of SLW at the top of the frontal mixed-
 390 phase clouds thus appears related to the dynamics of cloud-top convective cells (A. V. Ko-
 391 rolev & Mazin, 2003; A. Korolev et al., 2017) as within mid-latitude altocumulus (Heymsfield
 392 et al., 1991; Smith et al., 2009; P. A. Barrett et al., 2020). It is important to note that
 393 the lidar signal is fully attenuated by precipitation during the middle part of the event
 394 (see Figure S4), so there could have been SLW between 15 February 02 UTC and 16 Febru-
 395 ary 06 UTC. As a matter of fact, the highest LWP values estimated from the microwave
 396 radiometer were measured between 09 and 19 UTC 15 February (see next section). This

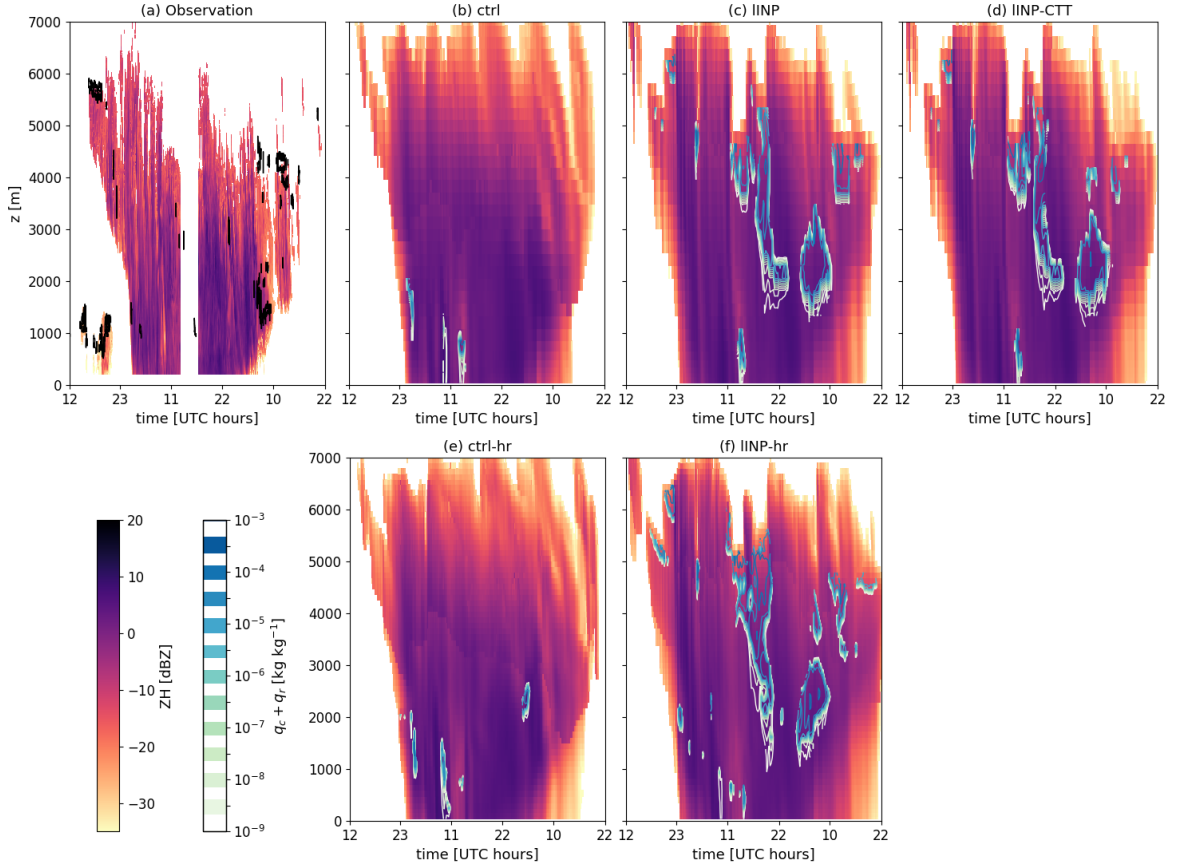


Figure 5. Time-height plot of the W-band reflectivity in MWACR observation (panel a) and as calculated from WRF simulations with the CR-SIM radar simulator (panels b-f). In panel a, black outlines locate regions where the MPL detects SLW. In panels b-f, yellow-to-blue contours show the mass mixing ratio of cloud liquid water (sum of cloud and rain droplets).

397 suggests the presence of SLW layers or patches within or at the top of the deep nimbo-
 398 stratus during this period, especially within or at the summit of layers with both high
 399 values of Doppler velocity and Doppler spectral width. The visual inspection of Doppler
 400 spectra indeed confirms the occurrence of elevated SLW layers during the precipitation
 401 period (Figure S5).

402 **3.2 Simulating the vertical structure of liquid-topped frontal mixed-phase**
 403 **clouds**

404 We now assess the ability of WRF to reproduce the observed cloud vertical struc-
 405 ture. Unlike the control (ctrl) simulation with the standard Morrison microphysical scheme,

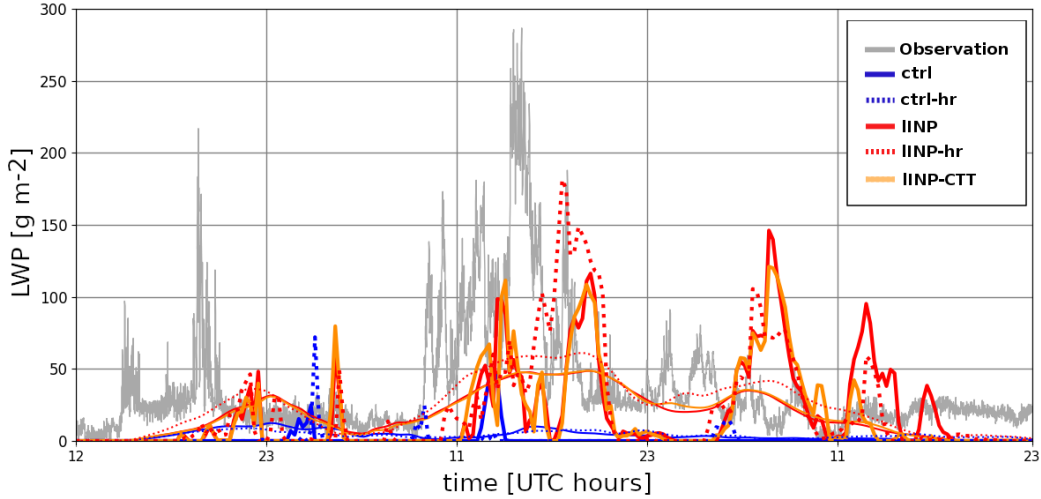


Figure 6. 14-16 February 2018 time series of the LWP above the Aurora Australis position (thick lines) and averaged over the whole domain excluding the relaxation zone near the domain's boundaries (thin lines) in WRF simulations. The LWP estimated from radiometer observations is added in grey line. Note that the LWP averaged over the whole domain from the IINP and IINP-CTT simulations are almost superimposed.

406 simulations using the empirical high-latitude Southern Ocean ice nucleation parameter-
 407 ization with a lower - but more realistic - INP concentration, are named 'IINP'. Simu-
 408 lations accounting for the cloud top turbulence parameterization are named with the '-
 409 CTT' suffix. Likewise, simulations run with the refined vertical grid in the troposphere
 410 are designated with the '-hr' suffix. By direct comparison with radiosoundings, we ver-
 411 ified that the vertical profiles of temperature, wind speed and wind direction in the simu-
 412 lations are reasonably well reproduced so that we can focus on the representation of
 413 cloud microphysics (not shown).

414 *3.2.1 Analysis of the control simulation*

415 Figure 5 shows the time height plot of the radar reflectivity and cloud liquid wa-
 416 ter content above the ship's position in the WRF simulations. It reveals that the ctrl sim-
 417 ulation reproduces the timing and the overall structure of the system reasonably well.
 418 However the local low-level clouds preceding the passage of the warm front are absent
 419 in the simulation above the ship position but similar local clouds form a few kilometers
 420 away (not shown). In addition, the model generally overestimates the cloud top height

421 particularly owing to the excessive ice nucleation at cold temperatures. More importantly,
 422 Figure 5b and the time series of the liquid water path in Figure 6 show that the ctrl con-
 423 figuration produces almost fully glaciated clouds. Refining the vertical grid in the mid-
 424 troposphere (ctrl-hr simulation) barely improves the production of liquid droplets. Note
 425 that changing the microphysical scheme to the one from Thompson et al. (2008) - that
 426 together with the Morrison scheme yields the best cloud liquid water content and sur-
 427 face radiative fluxes in previous Antarctic studies with WRF (Listowski & Lachlan-Cope,
 428 2017; Hines et al., 2019) - leads to the same conclusion (not shown). Note also that re-
 429 placing the INP formulation with the one from DeMott et al. (2010) in the deposition/condensation
 430 freezing nucleation parameterization leads to slightly more SLW in the lowest part of the
 431 clouds (where the temperature is greater than -15°C) but its overall amount remains
 432 strongly underestimated. It is also worth mentioning that unlike WRF in its standard
 433 configuration, the recent ERA5 reanalysis produces some cloud liquid content during this
 434 event, but not the correct amount nor at the correct location (at too low altitude and
 435 too warm temperature, see Figure S6 and Sect. 3 of the supporting information). This
 436 result concurs with the conclusions of Silber, Verlinde, Wang, et al. (2019) at two other
 437 Antarctic sites.

438 **3.2.2 Sensitivity experiments**

439 The empirical INP formulation leads to a significant increase in cloud liquid wa-
 440 ter content throughout the event. Such a conclusion holds not only at the ship's loca-
 441 tion but also for the whole simulation domain (thick and thin lines in Figure 6). Fur-
 442 ther analysis shows that this enhanced production of cloud liquid water over the whole
 443 model domain in the IINP simulation is associated with a strong decrease in cloud ice
 444 - owing to the less active heterogeneous nucleation process (Figure S7b,c) - and with a
 445 slight increase in snow mixing ratio in the mid-troposphere (Figure S7d) due to the WBF
 446 process. However the total condensed water content is not significantly modified (Fig-
 447 ure S7a).

448 The IINP simulation also exhibits sharp vertical gradients of condensate mixing ra-
 449 tio in the uppermost part of the clouds (Figure 5c) as well as vigorous cloud-top turbu-
 450 lence that is absent in the ctrl simulation (see the time-height plot of the TKE above
 451 the ship's position in WRF simulations in Figure 7). We will hereafter show that this

452 turbulence is triggered by a stronger buoyancy flux due to an enhance cloud-top radiative
 453 cooling.

454 Figure 8 shows vertical profiles of atmospheric variables for two particular times
 455 with clear liquid-topped altocumulus identified in observations (see vertical green lines
 456 in Figure 4). During the arrival of the warm front at 1730 UTC, 14 February 2018, the
 457 new INP parameterization makes WRF able to reach the saturation with respect to liq-
 458 uid in a layer around 5600 m whatever the vertical resolution employed. A thin SLW layer
 459 is therefore simulated at cloud top but its height is slightly underestimated compared
 460 to lidar observations. The analysis of vertical profiles of the source and loss terms of the
 461 ice and snow mixing ratio shows that below the SLW layer, ice crystals grow by vapor
 462 deposition and sediment (Figures 9b). The presence of liquid droplets at cloud top also
 463 enhances the radiative cooling, leading to an almost neutral vertical profile of potential
 464 temperature in agreement with radiosonde observation (Figure 8a). However, with the
 465 coarse vertical resolution employed in IINP, the liquid layer does not persist in time. When
 466 refining the vertical resolution (IINP-hr simulation), the resilience of the SLW layer dur-
 467 ing the warm front arrival (Figure 5f) is better reproduced - in agreement with the 1D-
 468 simulations of A. I. Barrett et al. (2017b). The altitude of the liquid layer gradually de-
 469 creases owing to the drying effect associated with cloud-top turbulent entrainment.

470 The IINP simulation does not reproduce the cloud top turbulence during this spe-
 471 cific period but IINP-hr exhibits both a resilient SLW layer and vigorous mixing (Fig-
 472 ure 8f). Activating the additional parameterization for cloud top turbulence enhance-
 473 ment in the low-resolution configuration (IINP-CTT simulation) helps generate turbu-
 474 lence in the upper part of the altocumulus. A similar conclusion can be drawn for the
 475 middle phase of the event (around 1200 UTC, 15 February, see Figure 7d). However, this
 476 parameterization does not improve the persistence of the SLW layer through time. Tur-
 477 bulence tends to thin the SLW layer out by mixing it with underlying and overlying drier
 478 air. As expected, increasing the ϕ parameter increases the TKE and ϵ but for $\phi \geq 0.1$,
 479 the mixing becomes too intense - with respect to the vertical resolution used - for SLW
 480 to survive over more than a few time steps (see Figure S8).

481 Similarly to the IINP-CTT simulation, the turbulence in the IINP-hr simulation
 482 tends to thin the SLW layer by mixing with drier air (Figure 8d). Interestingly, the par-
 483 allel analysis of the vertical profiles of the source and loss terms of SLW (Figures 9a,d)

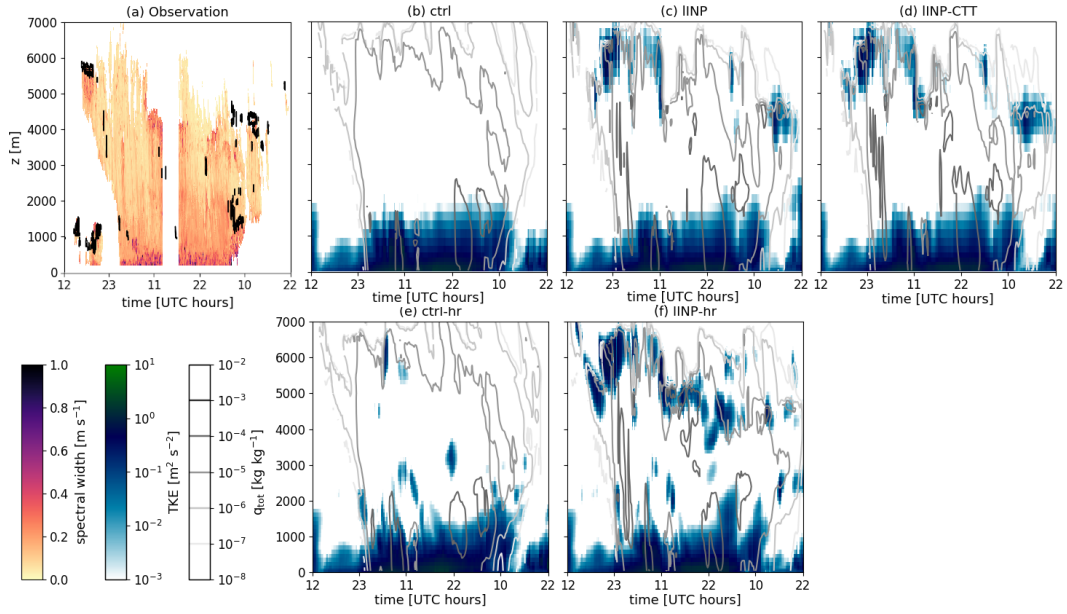


Figure 7. Panel a: Time-height plot of the spectral width in MWACR observation. Black outlines locate regions where the MPL detects SLW. Panels b-f: Time height plots of the TKE (color shading) and of the mass mixing ratio of cloud condensates (contours, sum of cloud droplet, cloud ice, snow, graupel and rain species, q_{tot}) above the ship position for different WRF simulations.

484 and of the temperature tendencies (Figures 9c,e) shows that SLW does not form in the
485 atmospheric layer where turbulent mixing cools the air. This is somewhat contradictory
486 with the conceptual model of mixed-phase altocumulus of (P. A. Barrett et al., 2020)
487 in which supercooled droplet condensation occurs within adiabatically cooled turbulent
488 updrafts. This aspect will be discussed in Sect. 4.3.

489 Analysis of profiles at 1230 UTC, 16 February (Figures 8g-l) generally concurs with
490 our main inferences regarding the performances of WRF at the beginning of the event.
491 We can still notice the absence of turbulence between 3000 and 4600 m in the IINP-hr
492 simulation which is explained by the cloud being too deep (see Figure 5f and Figure 8h)
493 - so an overestimated cloud top height and underestimated radiative cooling between 4000
494 and 4500 m (Figure 8k) - at this specific time. We do not have a clear explanation for
495 this bias but it seems that the deep nimbostratus stays too long over the ship location
496 and, interestingly, a thin SLW layer at around 4600 m is simulated during the end of the
497 16 February (Figure 5f). In absence of turbulence, the SLW layer in the IINP and IINP-
498 hr simulations - at this specific time - is too thick. It becomes more realistic later in the
499 day.

500 As previously mentioned, Sotiropoulou et al. (2020) suggest that secondary ice pro-
501 duction through ice particle collisional break-up might be an important process in coastal
502 Antarctic clouds. We have assessed the model sensitivity to this process on our study
503 case (details in Sect. 4 of the supporting information). Collisional break-up significantly
504 modifies the ice particle number concentration at temperature greater than -25°C but
505 the available observational dataset does not enable us to state whether this is truly ben-
506 efiticial to our simulations or not. In any case, a collisional break-up parameterization that
507 moderately increases the ice crystal number concentration is not detrimental to the sim-
508 ulation of SLW layers which is our main scope here.

509 **3.3 Cloud radiative effect**

510 Achieving the simulation of SLW layers substantially impacts the radiative fluxes
511 at the surface through changes in cloud albedo and optical depth. Comparison of the
512 surface downward longwave radiative flux above the ship reveals a better agreement when
513 the new INP parameterization is activated. The mean downwelling longwave flux value
514 between 1200 UTC, 14 February and 2200 UTC, 16 February equals 292.2 W m^{-2} in

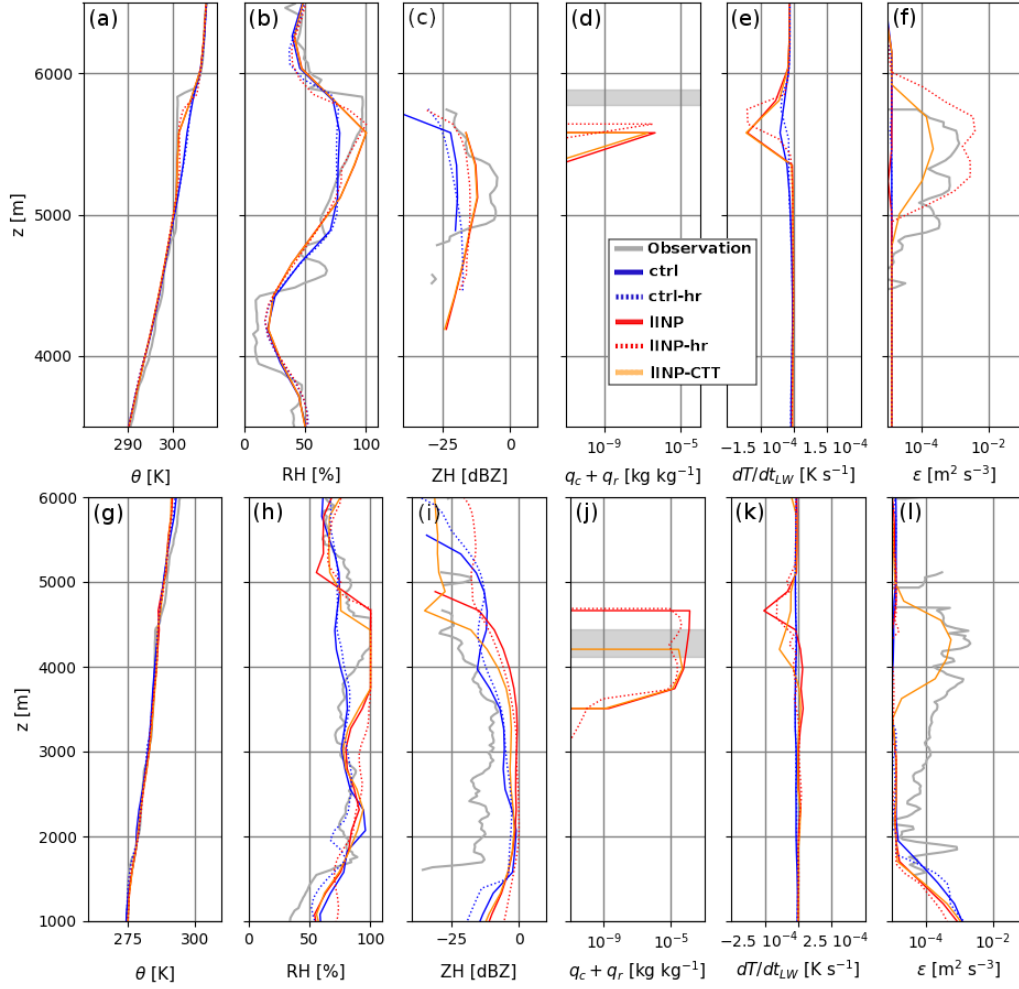


Figure 8. Vertical profiles of the potential temperature (a and g), relative humidity with respect to liquid (b and h), W-band radar reflectivity (c and i), liquid water content (sum of cloud droplets and rain drops, d and j), temperature tendency due to longwave radiative warming (e and k) and rate of turbulent kinetic energy dissipation (f and l) in observations (grey lines) and WRF simulations. Panels a-f refers to the 14 February 2018 at 1730 UTC while panels g-l refers to the 16 February 2018 at 1230 UTC. In panels a, b, g and h, observational data are from the closest-in-time radiosounding. In panels c, f, i and l, observations are from MWACR data. In panels d and j, the grey shading indicates the altitude range where the MPL detects SLW.

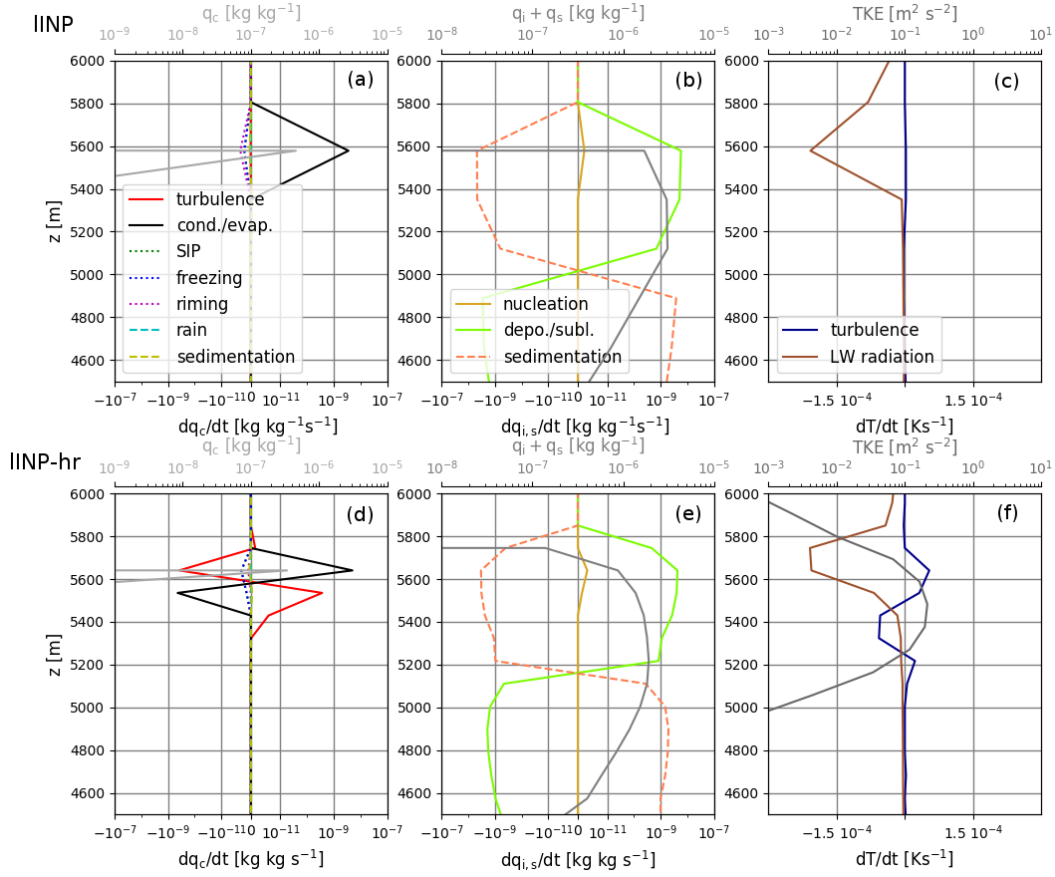


Figure 9. Vertical profiles at 1730 UTC, 14 February 2018, of different model variables for the IINP (panels a-c) and IINP-hr (panels d-f) WRF simulations. Panel a shows the cloud liquid water content (q_c , light grey line, top x-axis). Note that the rain mixing ratio q_r is negligible here. The different source/loss terms of cloud liquid water are also plotted in colored lines (note the logarithmic scale on the x-axes). 'turbulence' refers to turbulent mixing; 'cond./evap.' refers to droplet condensation or evaporation in a saturated/unsaturated atmosphere; 'SIP' refers to secondary ice production by splintering of droplets accreted on iced hydrometeors; 'riming' refers to the riming of iced precipitation; 'freezing' refers to the ice-nucleation through freezing (loss term for droplets), 'rain' refers to the autoconversion to rain and 'sedimentation' refers to the sedimentation of droplets. Panels b and e show the mass mixing ratio of the ice and snow species ($q_i + q_s$, grey line, top x-axis) and the relative tendencies due to ice nucleation (solid gold line), vapor deposition or sublimation (solid green line) and sedimentation (dashed orange line). Panels c and f: TKE (dark grey line, top x-axis), longwave radiative (brown) and turbulent (blue) heating rates. Note that the model does not simulate any TKE in panel c.

515 the observations, and 227.5 W m^{-2} , 237.6 W m^{-2} , 238.0 W m^{-2} , 241.1 W m^{-2} in the
 516 ctrl, IINP, IINP-CTT and IINP-hr simulations respectively. The value is however signif-
 517 icantly underestimated in all the simulations. Inspection of flux time series (not shown)
 518 reveals that this is mostly due to the absence of local low-level clouds just above the ship
 519 position and preceding the warm front. Such clouds indeed have a particularly strong
 520 warming effect. Comparison with model grid points in the vicinity of the ship that con-
 521 tains low-level clouds shows a substantially higher (up to 40 W m^{-2}) downward long-
 522 wave radiative flux at the arrival of the warm front. Likewise, the mean downwelling short-
 523 wave flux value between 1200 UTC, 14 February and 2200 UTC, 16 February, has been
 524 improved when activating the new INP parameterization mostly owing to the increase
 525 in cloud albedo when SLW is reproduced. While the mean observed value equals 160.4 W m^{-2} ,
 526 the simulated values are 187.8 W m^{-2} , 166.8 W m^{-2} , 167.5 W m^{-2} , 165.9 W m^{-2} in the
 527 ctrl, IINP, IINP-CTT and IINP-hr simulations respectively.

528 The changes in radiative fluxes substantially modify the cloud radiative effect (CRE)
 529 at the surface and the top of the atmosphere (TOA) during the event. Figure 10 shows
 530 the difference in CRE averaged over the whole study case between the IINP-hr (the con-
 531 figuration with the most realistic SLW layers) and ctrl simulations. At the TOA, the IINP-
 532 hr simulation exhibits more reflected shortwave radiation than the ctrl simulation (panel
 533 a), especially over the Southern Ocean because of an increase in cloud albedo, while the
 534 albedo discrepancy over snow and ice covered areas over the continent is less significant.
 535 This increase in albedo is also responsible for a decrease in the amount of shortwave ra-
 536 diation that reaches the ground surface (Figure 10d). On the other hand, the outgoing
 537 longwave radiative flux towards space diminishes due to colder cloud tops. Importantly,
 538 as liquid-bearing clouds are optically thicker, the IINP-hr simulation shows a much higher
 539 downward radiative flux ($+3.5 \text{ W m}^{-2}$ in average between 1200 UTC, 14 February and
 540 2200 UTC, 16 February), leading to a significant surface warming over the ice sheet sur-
 541 face with respect to the ctrl simulation (panel f). The same conclusions can be drawn
 542 for the IINP and IINP-CTT simulations. It is also worth noting that although our new
 543 parameterizations targeted mid-level clouds, inspection of vertical profiles of cloud prop-
 544 erties over the whole simulation domain shows that boundary-layer clouds are also - but
 545 to a lesser extent because of the warmer temperatures at lower altitude - modified with
 546 higher SLW content (Figure S7). Figure 10 thus integrates combined effects from changes
 547 on both mid-level and low-level clouds. Note also that the differences in CRE during the

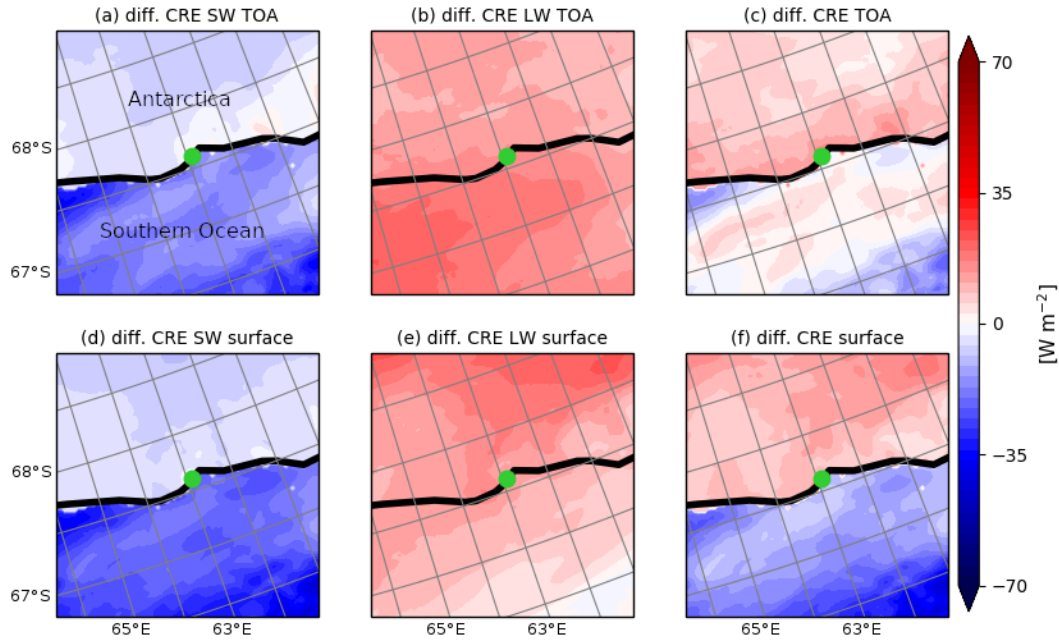


Figure 10. Difference in cloud radiative effect (CRE) averaged over the whole duration of the study case at the top of the atmosphere (TOA, top row) and at the surface (bottom row) between the IINP-hr and ctrl WRF simulations (3-km resolution innermost domain). Panels a and d show the shortwave (SW) component, panels b and e the longwave (LW) component, and panels c and f the total difference. The black line is the Antarctic landfall and the green dot locates Mawson station.

548 whole event duration shown in Figure 10 depend not only on changes in cloud phase but
 549 also on differences in cloud duration and cover. However, the CRE difference calculated
 550 during the middle-phase of the event, i.e. during a period in which the whole domain
 551 is covered by clouds in the two simulations, shows similar patterns as in Figure 10 but
 552 also a slightly lower magnitude of the differences (not shown). This suggests a dominant
 553 role of the change in cloud phase and a secondary but significant effect of the change in
 554 cloud duration and cover.

555 4 Discussion

556 4.1 Remaining shortcomings in our simulations

557 Despite improvements regarding the simulation of SLW layers, shortcomings remain
 558 in our simulations whatever the physical configuration used. Amongst the most strik-

559 ing biases, Figures 5 and 8h evidence an insufficient low-level sublimation during the last
 560 day of the event that is associated with an overestimation of the relative humidity when
 561 comparing with radiosoundings. This aspect can be improved when accounting for sec-
 562 ondary ice production through ice particle break-up (see Sect. 4 of the supporting in-
 563 formation).

564 Figure 6 also reveals an overall underestimation of the LWP in all the simulations
 565 as well as issues concerning the timing of the LWP peaks. Changing the intensity of the
 566 27-km resolution domain nudging or adding a nudging term on the temperature and/or
 567 the humidity fields has only little effect and does not alleviate those biases (not shown).
 568 A bias propagation from the ERA5 forcings into our inner simulation domains can thus
 569 not be excluded. Moreover, the absence of lidar measurements during the strong pre-
 570 cipitation phase that coincides with the highest LWP values prevents us from precisely
 571 evaluating the SLW representation during this period. Warm frontal systems often ex-
 572 hibit SLW layers or patches within deep nimbostratus associated with embedded con-
 573 vective cells (Keppas et al., 2018). The MWACR data shows high values (in magnitude)
 574 of the Doppler velocity and of the Doppler spectral width at the top of the nimbostra-
 575 tus between 9 and 13 UTC, 15 February, suggesting that intense cloud-top turbulent up-
 576 drafts may explain a significant part of the SLW production during this period. In ad-
 577 dition to turbulence, Gehring et al. (2020) show that within a nimbostratus over Korea,
 578 the large scale ascent corresponding to the warm conveyor belt of an extra-tropical cy-
 579 clone can be sufficient to create and sustain SLW. Comparing Figure 5 and Figure 7 shows
 580 that the IINP and IINP-hr simulations also exhibit SLW patches in the middle of the nim-
 581 bostratus (between about 2000 and 3500 m) i.e. in an altitude range with low values of
 582 TKE in the model and low values of spectral width in the MWACR data. Further in-
 583 spection of the resolved vertical velocity field in the model reveals that those SLW patches
 584 coincide with significant ascents (around $+0.1 - 0.2 \text{ m s}^{-1}$, not shown) but their real-
 585 ism cannot be assessed by comparison with our observational dataset. Hence, it remains
 586 difficult to disentangle whether the remaining biases in SLW quantity and timing dur-
 587 ing the precipitation period are due to a poor representation of the turbulence at the top
 588 of the nimbostratus and/or to the modeling of the large-scale ascent associated with syn-
 589 optic dynamics.

4.2 INP, turbulence, vertical resolution: what matters the most for achieving the simulation of SLW layers?

Our results highlight that without a realistic ice nucleation parameterization that accounts for the particularly low INP concentration over the high-latitude Southern Ocean, the representation of thin turbulent SLW layers and realistic SLW contents cannot be achieved. This conclusion holds whatever the vertical resolution tested, with or without additional subgrid turbulent mixing at cloud top. From the present analysis, the nature of the heterogeneous ice nucleation parameterization in atmospheric models, especially the representation of the limited INP numbers concentrations over this region, is an essential prerequisite to simulate the liquid phase in frontal mid-level mixed-phase clouds at high southern latitudes. Furthermore, it makes the model produce significant TKE near cloud top - which is missing in the ctrl simulation - due to enhanced radiative divergence. In our IINP and IINP-hr simulations, the persistence of the saturation with respect to liquid - and of the resulting SLW layer - mostly depends on a subtle competition between air cooling (primarily due to radiative divergence, see Figure 9) and moisture removal associated with the growth of ice crystals. Increasing the vertical resolution helps maintain the saturation because newly formed crystals get more easily separated from the liquid layer while falling. One can refer to A. I. Barrett et al. (2017b) for further discussion on the link between SLW resilience and model vertical resolution. In IINP, although SLW continues to form at 1730 UTC, the ice particle growth (Figure 9) makes the air under-saturated with respect to liquid after a few minutes. When the liquid layer disappears, the precipitating ice crystals falling towards the lower layer are not replaced by newly formed crystals and the total cloud water content decreases. The reappearance of SLW becomes impossible if other moistening processes (through advection for instance) do not come into play or until the temperature reaches the dew point through radiative cooling. In contrast in IINP-hr, the atmospheric layer between 5600 and 5750 m shows lower ice crystal concentration, a weaker vapor deposition on ice and significant radiative cooling (Figure 9), enabling the persistence of the SLW layer for several hours.

Even though the 100-m grid spacing in the mid-troposphere employed in the IINP-hr simulation helps reproduce the resilient thin SLW layers (at least qualitatively), it is probably still too coarse to accurately capture their fine vertical structure. Further increasing the vertical resolution in the WRF regional model would nonetheless not be rea-

sonable for computation cost and physical reasons, especially in the perspective of long climate runs. In line with A. I. Barrett et al. (2017b), further work on the parameterization of the subgrid vertical distribution of cloud condensates in mixed-phase conditions would thus be needed, but this is beyond the scope of the present paper.

Regarding the representation of turbulence, the underestimation of the occurrence and intensity of cloud top mixing at coarse vertical resolution could be anticipated and motivated the implementation of an additional source term in the TKE equation. The latter parameterization leads to better agreement with ϵ estimations from Doppler radar measurements during the front arrival and during the course of the event. However and unlike the increase in vertical resolution, this parameterization does not help sustain the SLW layer and conversely it can amplify its depletion if the ϕ coefficient is set to a too high value. This apparent second role of turbulence for SLW resilience may be co-incidental since the state-of-the-art MYNN local turbulent mixing scheme is likely inadequate for reproducing the top-down convection at mid-level cloud top. This may even question the physical representation of cloud droplet formation and growth in the model (see next section).

4.3 The pressing need of revisiting the parameterization of cloud top turbulence

One aspect that particularly deserves further discussion is the representation of cloud top turbulence in the model. We have shown that in some cases, an additional source term in the TKE equation, compensating for the incomplete reproduction of the radiative cooling, helps obtain some TKE at cloud top. However the *local* TKE generation by buoyancy fluxes in the IINP-CTT and IINP-hr (and to a lesser extent in the IINP) simulations lead to a patch of TKE (or ϵ) that is vertically centered around cloud top liquid and that unrealistically diminishes the temperature inversion (Figure 8a,f and 9f). Even though our estimation of ϵ only applies where the radar detects signal in the cloud, the sharp temperature inversion in the observations suggests that turbulent motions mostly occur within and below the cloud. Using turbulence data from aircraft measurements, P. A. Barrett et al. (2020) show that the TKE maximum occurs several hundred meters below typical mixed-phase altocumulus top. Indeed, the turbulence structure within altocumulus consists of shallow small-scale eddies at cloud top below which an organized Rayleigh Bénard-type convection takes place with negatively buoyant air parcels that

655 descend through the cloud layer in coherent downdrafts and force upward motion through
656 mass continuity (Schmidt et al., 2014; P. A. Barrett et al., 2020). Subrotor circulations
657 associated with ice virga shafts may also participate in the mixing below the cloud. Over-
658 all the organized convection triggered at cloud-top cannot be represented by the typi-
659 cal local turbulent mixing schemes used in atmospheric models like MYNN or all the cur-
660 rent 1.5-order planetary boundary layer schemes in WRF. Moreover, the adiabatic cool-
661 ing, the saturation with respect to liquid and the growth and vertical transport of droplets
662 only occurs within updrafts. Considering each model layer as homogeneous in terms of
663 temperature and humidity necessarily prevents the proper representation of the dynam-
664 ics of turbulent mixed-phase clouds. Albeit satisfactory compared to simulations with
665 the standard version of WRF, the representation of SLW layers in the IINP-hr config-
666 uration may result from a partially non-physical interplay between turbulence and mi-
667 crophysics. Adapting a non-local turbulent mixing parameterization based on a mass-
668 flux scheme that treats separately a ‘lifting’ fraction and a ‘subsiding’ fraction of each
669 mesh (see Hourdin et al., 2019 for instance) might be an interesting approach to tackle
670 this issue in the future. Such types of scheme are already active in many atmospheric
671 models to parameterize the mixing in convective ground-based boundary layers but they
672 are not active aloft.

673 **5 Conclusions**

674 By using remotely-sensed measurements obtained during the MARCUS campaign,
675 we have evaluated the ability of the WRF regional atmospheric model to reproduce the
676 thin and turbulent layers of SLW at the top of frontal mixed-phase clouds over the high-
677 latitude Southern Ocean.

678 While the control simulation did not exhibit any cloud liquid water above the bound-
679 ary layer, we found that modifying the ice nucleation parameterization through the im-
680 plementation of a truly representative INP concentrations measured around the time of
681 the event considerably improved our simulation results. We can thus infer that adapt-
682 ing the ice nucleation parameterization to the particularly pristine conditions prevail-
683 ing over the Southern Ocean is essential for atmospheric models running over this re-
684 gion, in agreement with the conclusions of Vergara-Temprado et al. (2018). Refining the
685 vertical resolution in the troposphere led to slightly higher liquid water content, but, first
686 and foremost, it allowed us to simulate more stable-in-time SLW layers and to simulate

687 vigorous and frequent turbulence within clouds. At coarse vertical resolution, the enhanced
688 cloud-top radiative cooling associated with the cloud droplet production still made it pos-
689 sible to simulate some turbulence in mid-level clouds. An additional parameterization
690 for cloud-top turbulence generation further led to more realistic comparison with radar
691 estimations of the TKE dissipation rate during specific periods like during the arrival
692 of the warm front, but it does not help sustain the SLW layer at altocumulus top.

693 Our changes in the model physics considerably modified the simulated CRE dur-
694 ing the event. Amongst the most prominent signals, we could point out a pronounced
695 decrease in CRE at the ocean surface due to more shortwave radiation reflected toward
696 space by the more realistic SLW layers and an increase in CRE at the ice sheet surface
697 owing to an enhanced downward longwave radiative flux. Despite improvements regard-
698 ing the simulation of SLW, the timing and the correct quantity of the LWP were still not
699 satisfactorily reproduced, questioning the representation of cloud-top liquid layers and/or
700 embedded liquid patches within clouds during the precipitation period.

701 Albeit very promising, our new ice nucleation parameterization based on an INP
702 concentration formulation that only depends on temperature cannot be fully satisfac-
703 tory since it does not account for the true link between aerosol populations and ice nu-
704 cleation. This calls for a future more accurate aerosol-aware formulation for INPs in the
705 high-latitude Southern Ocean.

706 Importantly, the way turbulent mixing at cloud top is represented - and hence the
707 physical representation of liquid droplet condensation and growth in mixed-phase clouds
708 - remains questionable since the local 1.5 order turbulent mixing parameterization does
709 not properly account for non-local convective transport and since it does not treat sep-
710 arately the respective evolution of rising and subsiding air parcels. This invites further
711 parameterization development targeting the top-down convection at cloud-top, taking,
712 for instance, inspiration from mass-flux schemes used to treat the mixing by thermal plumes
713 in convective boundary-layers.

714 Although our work has focused on one single event, Alexander et al. (2020) found
715 that the cloud/precipitation structure and the ubiquitous occurrence of SLW layers dur-
716 ing this event share many similarities with other synoptic cyclone events over the high-
717 latitude Southern Ocean. Our conclusions regarding the model performances and the nec-

718 essary changes in the cloud parameterization can thus be very likely extended to the over-
719 all representation of mid-level clouds over the Southern Ocean, at least in summer.

720 Last but not least, our work does not enable us to draw any robust conclusions about
721 the ability of WRF to reproduce the low-level mixed-phase clouds which have strong ra-
722 diative effects at the surface in our study case and which explain the major part of the
723 radiative bias over the Southern Ocean in CMIP models. Future studies are thus needed
724 to broach this aspect, tackling in particular the coupling - or decoupling - between clouds
725 and the ocean surface, the effect of surface evaporation and the interactions with the boundary-
726 layer dynamics.

727 **Acknowledgments**

728 This work was funded by the EPFL-LOSUMEA project. The contribution of S.A. was
729 supported through Australia Antarctic Science projects 4292 and 4387. P.D. acknowl-
730 edges support from the U.S. Department of Energy's (DOE) Atmospheric System Re-
731 search, an Office of Science Biological and Environmental Research program, under Grant
732 No. DE-SC0018929, and use of data obtained from the DOE Atmospheric Radiation Mea-
733 surement (ARM) User Facility. We thank Constantino Listowski, Jean-Baptiste Madeleine,
734 Noémie Planat, Michael Lehning and Varun Sharma for fruitful discussions, Josué Gehring
735 for his help for the turbulence dissipation rate estimations from radar data and Jay Mace
736 for helping calibrate the radar measurements. We also gratefully thank Kevin Barry for
737 assisting with processing of the INP samples. Technical, logistical and ship support for
738 MARCUS were provided by the AAD through Australian Antarctic Science projects 4292
739 and 4387 and we thank Steven Whiteside, Lloyd Symonds, Rick van den Enden, Peter
740 de Vries, Chris Young and Chris Richards for assistance. We also thank four anonymous
741 reviewers whose insightful comments that helped to improve the manuscript. Raw MAR-
742 CUS data are freely available from the ARM data archive (<https://www.arm.gov/data>)
743 and MARCUS experiment webpage (<https://www.arm.gov/research/campaigns/amf2017marcus>).
744 The processed lidar and radiometer data used in this paper have been made available
745 on the Australian Antarctic Data Centre (Alexander, 2020). Likewise, the LWP data used
746 in this study are available here: https://atmos.uw.edu/~roj/MARCUS_and_MICRE/. ERA5
747 reanalyses can be freely downloaded from the Copernicus climate data store ([https://](https://cds.climate.copernicus.eu)
748 cds.climate.copernicus.eu). The original WRF code is open source. All the simu-
749 lation data presented in this paper are available upon request to the authors. The new

750 WRF topography file from the Reference Elevation Model of Antarctica dataset will be
751 made freely available if the paper is accepted.

752 References

- 753 Alexander, S. P. (2020). Derived data products produced from marcus cyclone ob-
754 servations, january-february, 2018, ver. 1. *Australian Antarctic Data Centres*,
755 *Accessed: 2020-10-28*. doi: 10.4225/15/58eedd2fd5a6b
- 756 Alexander, S. P., McFarquhar, G., Marchand, R., Protat, A., Vignon, E., Mace,
757 G. G., & Klekociuk, A. R. (2020). Mixed-phase clouds over the southern ocean
758 cyclones and cloud systems observed poleward of 64°S by ship-based cloud
759 radar and lidar. *Journal of Geophysical Research: Atmospheres*, in revision.
- 760 Alexander, S. P., & Protat, A. (2018). Cloud properties observed from the sur-
761 face and by satellite at the northern edge of the southern ocean. *Jour-
762 nal of Geophysical Research: Atmospheres*, 123(1), 443-456. doi: 10.1002/
763 2017JD026552
- 764 Andronache, C., & coauthors. (2017). *Mixed phase clouds : observations and model-
765 ing*. elsevier edition. doi: 10.106/B978-0-12-810549-8.00007-6
- 766 Barrett, A. I., Hogan, R. J., & Forbes, R. M. (2017a). Why are mixed-phase al-
767 tocumulus clouds poorly predicted by large-scale models? part 1. physical
768 processes. *Journal of Geophysical Research: Atmospheres*, 122(18), 9903-9926.
769 doi: 10.1002/2016JD026321
- 770 Barrett, A. I., Hogan, R. J., & Forbes, R. M. (2017b). Why are mixed-phase al-
771 tocumulus clouds poorly predicted by large-scale models? part 1. vertical
772 resolution sensitivity and parameterization. *Journal of Geophysical Research:
773 Atmospheres*, 122(18), 9922-9944. doi: 10.1002/2016JD026322
- 774 Barrett, P. A., Blyth, A., Brown, P. R. A., & Abel, S. J. (2020). The structure
775 of turbulence and mixed-phase cloud microphysics in a highly supercooled
776 altocumulus cloud. *Atmospheric Chemistry and Physics*, 20(4), 1921-1939.
777 Retrieved from <https://www.atmos-chem-phys.net/20/1921/2020/> doi:
778 10.5194/acp-20-1921-2020
- 779 Bigg, E. K. (1953). The supercooling of water. *Proceedings of the Physical Society*.
780 *Section B*, 66(8), 688.
- 781 Bodas-Salcedo, A., Andrews, T., Karmalkar, A. V., & Ringer, M. A. (2016). Cloud

- 782 liquid water path and radiative feedbacks over the southern ocean. *Geophysical*
783 *Research Letters*, *43*(20), 10,938-10,946. doi: 10.1002/2016GL070770
- 784 Bodas-Salcedo, A., Williams, K. D., Ringer, M. A., Beau, I., Cole, J. N. S.,
785 Dufresne, J.-L., ... Yokohata, T. (2014). Origins of the solar radiation bi-
786 ases over the southern ocean in cmip2 models. *Journal of Climate*, *27*(1),
787 41-56. doi: 10.1175/JCLI-D-13-00169.1
- 788 Brient, F., Couvreur, F., Villefranque, N., Rio, C., & Honnert, R. (2019). Object-
789 oriented identification of coherent structures in large eddy simulations: Import-
790 tance of downdrafts in stratocumulus. *Geophysical Research Letters*, *46*(5),
791 2854-2864. doi: 10.1029/2018GL081499
- 792 Cooper, W. A. (1986). Ice initiation in natural clouds. *Meteor Mon*, *21*, 29-32.
- 793 Deardoff, J. W. (1972). On the entrainment rate of a stratocumulus-topped mixed
794 layer. *Q J R Meteorol Soc*, *102*, 503-583.
- 795 de Boer, G., Hashino, T., Tripoli, G. J., & Eloranta, E. W. (2013). A numerical
796 study of aerosol influence on mixed-phase stratiform clouds through modula-
797 tion of the liquid phase. *Atmospheric Chemistry and Physics*, *13*(4), 1733-
798 1749. doi: 10.5194/acp-13-1733-2013
- 799 DeMott, P. J., Hill, T. C., McCluskey, C. S., Prather, K. A., Collins, D. B., Sullivan,
800 R. C., ... others (2016). Sea spray aerosol as a unique source of ice nucle-
801 ating particles. *Proceedings of the National Academy of Sciences*, *113*(21),
802 5797-5803.
- 803 DeMott, P. J., Hill, T. C., & McFarquhar, G. (2018). Measurements of aerosols,
804 radiation, and clouds over the southern ocean (marcus) ice nucleating parti-
805 cle measurements field campaign report. *Ed. by Robert Stafford, ARM user*
806 *facility, DOE/SC-ARM-18-031*.
- 807 DeMott, P. J., Prenni, A. J., Liu, X., Kreidenweis, S. M., Petters, M. D., Twohy,
808 C. H., ... Rogers, D. (2010). Predicting global atmospheric ice nuclei distri-
809 butions and their impacts on climate. *Proceedings of the National Academy of*
810 *Sciences*, *107*(25), 11217-11222.
- 811 Flato, G., & coauthors. (2013). Evaluation of climate models. *Climate Change 2013:*
812 *The Physical Science Basis, T. F. Stocker et al., Eds., Cambridge University*
813 *Press*, 741-866.
- 814 Forbes, R., & Ahlgrimm, M. (2014). On the representation of high-latitude bound-

- 815 ary layer mixed-phase cloud in the ecmwf global model. *Mon Wea Rev*, *142*,
816 3425–3445.
- 817 Furtado, K., Field, P. R., Boutle, I. A., Morcrette, C. R., & Wilkinson, H. (2016).
818 A physically based subgrid parametrization for the production and mainte-
819 nance of mixed-phase clouds in a general circulation model. *J Atmos Sci*, *73*,
820 279-291. doi: 10.1175/JAS-D-15-0021.1
- 821 Gehring, J., Oertel, A., Vignon, E., Jullien, N., Besic, N., & Berne, A. (2020).
822 Microphysics and dynamics of snowfall associated to a warm conveyor belt
823 over korea. *Atmospheric Chemistry and Physics*, *2020*, 1–35. Retrieved
824 from <https://www.atmos-chem-phys-discuss.net/acp-2019-1173/> doi:
825 10.5194/acp-2019-1173
- 826 Gettelman, A., Hannay, C., Bacmeister, J. T., Neale, R. B., Pendergrass, A. G.,
827 Danabasoglu, G., ... Mills, M. J. (2019). High climate sensitivity in the com-
828 munity earth system model version 2 (cesm2). *Geophysical Research Letters*,
829 *46*(14), 8329-8337. doi: 10.1029/2019GL083978
- 830 Ghonima, M. S., Yang, H., Kim, C. K., Heus, T., & Kleissl, J. (2017). Evaluation
831 of wrf scm simulations of stratocumulus-topped marine and coastal bound-
832 ary layers and improvements to turbulence and entrainment parameteriza-
833 tions. *Journal of Advances in Modeling Earth Systems*, *9*(7), 2635-2653. doi:
834 10.1002/2017MS001092
- 835 Gilbert, E., Orr, A., King, J. C., Renfrew, I. A., Lachlan-Cope, T., Field, P. F., &
836 Boutle, I. A. (2020). Summertime cloud phase strongly influences surface
837 melting on the larsen c ice shelf, antarctica. *Quarterly Journal of the Royal*
838 *Meteorological Society*, *n/a*(n/a). doi: 10.1002/qj.3753
- 839 Grazioli, J., Genthon, C., Boudevillain, B., Duran-Alarcon, C., Del Guasta, M.,
840 Madeleine, J.-B., & Berne, A. (2017). Measurements of precipitation in du-
841 mont d'urville, adélie land, east antarctica. *The Cryosphere*, *11*(4), 1797-1811.
842 doi: 10.5194/tc-11-1797-2017
- 843 Grenier, H., & Bretherton, C. S. (2001). A moist pbl parameterization for large-
844 scale models and its application to subtropical cloud-topped marine boundary
845 layers. *Monthly weather review*, *129*(3), 357–377.
- 846 Guo, Z., Wang, M., Larson, V. E., & Zhou, T. (2019). A cloud top radiative cooling
847 model coupled with clubb in the community atmosphere model: Description

- 848 and simulation of low clouds. *Journal of Advances in Modeling Earth Systems*,
849 *11*(4), 979-997. doi: 10.1029/2018MS001505
- 850 Hersbach, H., Bell, B., Berrisford, P., Hirahara, S., Horányi, A., Muñoz-Sabater, J.,
851 ... Thépaut, J.-N. (2020). The era5 global reanalysis. *Quarterly Journal of*
852 *the Royal Meteorological Society*, *n/a*(n/a). doi: 10.1002/qj.3803
- 853 Heymsfield, A. J., Miloshevich, L. M., Slingo, A., Sassen, K., & Starr, D. O. (1991).
854 An observational and theoretical study of highly supercooled altocumulus.
855 *Journal of the atmospheric sciences*, *48*(7), 923–945.
- 856 Hines, K. M., & Bromwich, D. H. (2008). Development and testing of polar weather
857 research and forecasting (wrf) model. part i: Greenland ice sheet meteorology.
858 *Monthly Weather Review*, *136*(6), 1971-1989. doi: 10.1175/2007MWR2112.1
- 859 Hines, K. M., Bromwich, D. H., Wang, S.-H., Silber, I., Verlinde, J., & Lubin, D.
860 (2019). Microphysics of summer clouds in central west antarctica simulated
861 by the polar weather research and forecasting model (wrf) and the antarctic
862 mesoscale prediction system (amps). *Atmospheric Chemistry and Physics*,
863 *19*(19), 12431–12454. doi: 10.5194/acp-19-12431-2019
- 864 Hogan, R. J., Francis, P. N., Flentje, H., Illingworth, A. J., Quante, M., & Pelon, J.
865 (2003). Characteristics of mixed-phase clouds: Part i. lidar, radar and aircraft
866 observations from clare98. *Q J R Meteorol Soc*, *129*, 2089-2116.
- 867 Hourdin, F., Jam, A., Rio, C., Couvreux, F., Sandu, I., Lefebvre, M.-P., ... Idelkadi,
868 A. (2019). Unified parameterization of convective boundary layer transport
869 and clouds with the thermal plume model. *Journal of Advances in Modeling*
870 *Earth Systems*, *11*(9), 2910-2933. doi: 10.1029/2019MS001666
- 871 Howat, I. M., Porter, C., Smith, B. E., Noh, M.-J., & Morin, P. (2019). The refer-
872 ence elevation model of antarctica. *The Cryosphere*, *13*(2), 665–674. doi: 10
873 .5194/tc-13-665-2019
- 874 Hyder, P., Edwards, J. M., Allan, R. P., Hewitt, H. T., Bracegirdle, T. J., Gregory,
875 J. M., ... others (2018). Critical southern ocean climate model biases traced
876 to atmospheric model cloud errors. *Nature communications*, *9*.
- 877 Jullien, N., Vignon, E., Sprenger, M., Aemisegger, F., & Berne, A. (2020). Synoptic
878 conditions and atmospheric moisture pathways associated with virga and pre-
879 cipitation over coastal adélie land in antarctica. *The Cryosphere*, *14*(5), 1685–
880 1702. Retrieved from <https://tc.copernicus.org/articles/14/1685/2020/>

- 881 doi: 10.5194/tc-14-1685-2020
- 882 Kanji, Z. A., Ladino, L. A., Wex, H., Boose, Y., Burkert-Kohn, M., Cziczo, D. J.,
883 & Krämer, M. (2017). Overview of ice nucleating particles. *Meteorological*
884 *Monographs*, 58, 1.1-1.33. doi: 10.1175/AMSMONOGRAPHS-D-16-0006.1
- 885 Kawai, H., Yukimoto, S., Koshiro, T., Oshima, N., Tanaka, T., Yoshimura, H., &
886 Nagasawa, R. (2019). Significant improvement of cloud representation in
887 the global climate model mri-esm2. *Geoscientific Model Development*, 12(7),
888 2875–2897. doi: 10.5194/gmd-12-2875-2019
- 889 Kay, J. E., Wall, C., Yettella, V., Medeiros, B., Hannay, C., Caldwell, P., & Bitz, C.
890 (2016). Global climate impacts of fixing the southern ocean shortwave radia-
891 tion bias in the community earth system model (cesm). *Journal of Climate*,
892 29(12), 4617-4636. doi: 10.1175/JCLI-D-15-0358.1
- 893 Keppas, S. C., Crosier, J., Choulaton, T. W., & Bower, K. N. (2018). Microphys-
894 ical properties and radar polarimetric features within a warm front. *Monthly*
895 *Weather Review*, 146(7), 2003-2022. doi: 10.1175/MWR-D-18-0056.1
- 896 King, J. C., Gadian, A., Kirchgassner, A., Kuipers Munneke, P., Lachlan-Cope,
897 T. A., Orr, A., ... Weeks, M. (2015). Validation of the summertime surface
898 energy budget of larsen c ice shelf (antarctica) as represented in three high-
899 resolution atmospheric models. *Journal of Geophysical Research: Atmospheres*,
900 120(4), 1335-1347. doi: 10.1002/2014JD022604
- 901 Kollias, P., Puigdomènech Treserras, B., & Protat, A. (2019). Calibration of the
902 2007–2017 record of atmospheric radiation measurements cloud radar observa-
903 tions using cloudsat. *Atmospheric Measurement Techniques*, 12(9), 4949–4964.
904 Retrieved from <https://www.atmos-meas-tech.net/12/4949/2019/> doi:
905 10.5194/amt-12-4949-2019
- 906 Korolev, A., McFarquhar, G., Field, P. R., Franklin, C., Lawson, P., Wang, Z., ...
907 Wendisch, M. (2017). Mixed-phase clouds: Progress and challenges. *Meteo-*
908 *rological Monographs*, 58, 5.1-5.50. doi: 10.1175/AMSMONOGRAPHS-D-17
909 -0001.1
- 910 Korolev, A. V., & Mazin, I. P. (2003). Supersaturation of water vapor in
911 clouds. *Journal of the Atmospheric Sciences*, 60(24), 2957-2974. doi:
912 10.1175/1520-0469(2003)060<2957:SOWVIC>2.0.CO;2
- 913 Lenaerts, J. T. M., Van Tricht, K., Lhermitte, S., & L'Ecuyer, T. S. (2017). Polar

- 914 clouds and radiation in satellite observations, reanalyses, and climate models.
915 *Geophysical Research Letters*, 44(7), 3355-3364. doi: 10.1002/2016GL072242
- 916 Lenderink, G., & Holtslag, A. (2000). Evaluation of the kinetic energy approach for
917 modeling turbulent fluxes in stratocumulus. *Monthly weather review*, 128(1),
918 244–258.
- 919 Listowski, C., Delanoë, J., Kirchgaessner, A., Lachlan-Cope, T., & King, J. (2019).
920 Antarctic clouds, supercooled liquid water and mixed-phase investigated with
921 dardar: geographical and seasonal variations. *Atmospheric Chemistry and
922 Physics Discussions*, 2019, 1–52. doi: 10.5194/acp-2018-1222
- 923 Listowski, C., & Lachlan-Cope, T. (2017). The microphysics of clouds over
924 the Antarctic peninsula – part 2: modelling aspects within polar wrf. *At-
925 mospheric Chemistry and Physics*, 17(17), 10195–10221. doi: 10.5194/
926 acp-17-10195-2017
- 927 Lock, A. P. (1998). The parametrization of entrainment in cloudy boundary layers.
928 *Q J R Meteorol Soc*, 124, 2729-2753.
- 929 Lock, A. P., Brown, A. R., Bush, M. R., Martin, G. M., & Smith, R. N. B. (2000).
930 A new boundary layer mixing scheme. part i: Scheme description and single-
931 column model tests. *Monthly Weather Review*, 128(9), 3187-3199. doi:
932 10.1175/1520-0493(2000)128<3187:ANBLMS>2.0.CO;2
- 933 Lubin, D., Zhang, D., Silber, I., Scott, R. C., Kalogeras, P., Battaglia, A., . . . Vogel-
934 mann, A. M. (2020, 07). AWARE: The Atmospheric Radiation Measurement
935 (ARM) West Antarctic Radiation Experiment. *Bulletin of the American Mete-
936 orological Society*, 101(7), E1069-E1091. doi: 10.1175/BAMS-D-18-0278.1
- 937 Mace, G. G. (2010). Cloud properties and radiative forcing over the mar-
938 itime storm tracks of the southern ocean and north atlantic derived from
939 a-train. *Journal of Geophysical Research: Atmospheres*, 115(D10). doi:
940 10.1029/2009JD012517
- 941 Marchand, R., Ackerman, T., Westwater, E. R., Clough, S. A., Cady-Pereira, K., &
942 Liljegren, J. C. (2003). An assessment of microwave absorption models and
943 retrievals of cloud liquid water using clear-sky data. *Journal of Geophysical
944 Research: Atmospheres*, 108(D24). doi: 10.1029/2003JD003843
- 945 Mason, S., Jakob, C., Protat, A., & Delanoë, J. (2014). Characterizing ob-
946 served midtopped cloud regimes associated with southern ocean short-

- 947 wave radiation biases. *Journal of Climate*, 27(16), 6189-6203. doi:
948 10.1175/JCLI-D-14-00139.1
- 949 McCluskey, C. S., Hill, T. C. J., Humphries, R. S., Rauker, A. M., Moreau, S.,
950 Strutton, P. G., ... DeMott, P. J. (2018). Observations of ice nucleating
951 particles over southern ocean waters. *Geophysical Research Letters*, 45(21),
952 11,989-11,997. doi: 10.1029/2018GL079981
- 953 Mellado, J. P. (2017). Cloud-top entrainment in stratocumulus clouds. *Annual*
954 *Review of Fluid Mechanics*, 49(1), 145-169. doi: 10.1146/annurev-fluid-010816
955 -060231
- 956 Meyers, M. P., DeMott, P. J., & Cotton, W. R. (1992). New primary ice-nucleation
957 parameterizations in an explicit cloud model. *Journal of Applied Meteorology*,
958 31(7), 708-721. doi: 10.1175/1520-0450(1992)031<0708:NPINPI>2.0.CO;2
- 959 Morrison, H., Curry, D. A., & Khvorostyanov, V. I. (2005). A new double-moment
960 microphysics parametrization for application in cloud and climate models. part
961 i: Description. *J Atmos Sci*, 62, 1665-1677. doi: 10.1175/jas3446
- 962 Morrison, H., De Boer, G., Feingold, G., Harrington, J., Shupe, M. D., & Sulia, K.
963 (2012). Resilience of persistent arctic mixed-phase clouds. *Nature Geoscience*,
964 5(1), 11.
- 965 Nicolas, J. P., Vogelmann, A. M., Scott, R. C., Wilson, A. B., Cadetdu, M. P.,
966 Bromwich, D. H., ... others (2017). January 2016 extensive summer melt in
967 west antarctica favoured by strong el niño. *Nature communications*, 8, 15799.
- 968 O'Shea, S. J., Choularton, T. W., Flynn, M., Bower, K. N., Gallagher, M.,
969 Crosier, J., ... Lachlan-Cope, T. (2017). In situ measurements of cloud
970 microphysics and aerosol over coastal antarctica during the mac cam-
971 paign. *Atmospheric Chemistry and Physics*, 17(21), 13049-13070. doi:
972 10.5194/acp-17-13049-2017
- 973 Oue, M., Tatarevic, A., Kollias, P., Wang, D., Yu, K., & Vogelmann, A. M. (2020).
974 The cloud-resolving model radar simulator (cr-sim) version 3.3: description
975 and applications of a virtual observatory. *Geoscientific Model Development*,
976 13(4), 1975-1998. doi: 10.5194/gmd-13-1975-2020
- 977 Paukert, M., & Hoose, C. (2014). Modeling immersion freezing with aerosol-
978 dependent prognostic ice nuclei in arctic mixed-phase clouds. *Journal of Geo-*
979 *physical Research: Atmospheres*, 119(14), 9073-9092. Retrieved from <https://>

- 980 agupubs.onlinelibrary.wiley.com/doi/abs/10.1002/2014JD021917 doi:
981 10.1002/2014JD021917
- 982 Protat, A., Schulz, E., Rikus, L., Sun, Z., Xiao, Y., & Keywood, M. (2017). Ship-
983 borne observations of the radiative effect of southern ocean clouds. *J Geophys*
984 *Res Atmos*, *121*(318328). doi: 10.1002/2016JD026061
- 985 Ricaud, P., Del Guasta, M., Bazile, E., Azouz, N., Lupi, A., Durand, P., . . . Gri-
986 gioni, P. (2020). Supercooled liquid water cloud observed, analysed,
987 and modelled at the top of the planetary boundary layer above dome c,
988 antarctica. *Atmospheric Chemistry and Physics*, *20*(7), 4167–4191. Re-
989 trieved from <https://www.atmos-chem-phys.net/20/4167/2020/> doi:
990 10.5194/acp-20-4167-2020
- 991 Sato, K., Inoue, J., Alexander, S. P., McFarquhar, G., & Yamazaki, A. (2018). Im-
992 proved reanalysis and prediction of atmospheric fields over the southern ocean
993 using campaign-based radiosonde observations. *Geophysical Research Letters*,
994 *45*(20), 11,406–11,413. doi: 10.1029/2018GL079037
- 995 Schmidt, J. M., Flatau, P. J., & Yates, R. D. (2014). Convective cells in altocu-
996 mulus observed with a high-resolution radar. *Journal of the Atmospheric Sci-*
997 *ences*, *71*(6), 2130–2154. doi: 10.1175/JAS-D-13-0172.1
- 998 Sedlar, J., Shupe, M. D., & Tjernström, M. (2012). On the Relationship be-
999 tween Thermodynamic Structure and Cloud Top, and Its Climate Sig-
1000 nificance in the Arctic. *Journal of Climate*, *25*(7), 2374–2393. doi:
1001 10.1175/JCLI-D-11-00186.1
- 1002 Silber, I., Fridlind, A. M., Verlinde, J., Ackerman, A. S., Chen, Y.-S., Bromwich,
1003 D. H., . . . Eloranta, E. W. (2019). Persistent supercooled drizzle at
1004 temperatures below -25c observed at mcmurdo station, antarctica. *Jour-*
1005 *nal of Geophysical Research: Atmospheres*, *124*(20), 10878–10895. doi:
1006 10.1029/2019JD030882
- 1007 Silber, I., Verlinde, J., Cadeddu, M., Flynn, C. J., Vogelmann, A. M., & Eloranta,
1008 E. W. (2019). Antarctic cloud macrophysical, thermodynamic phase, and
1009 atmospheric inversion coupling properties at mcmurdo station—part ii: Radia-
1010 tive impact during different synoptic regimes. *Journal of Geophysical Research:*
1011 *Atmospheres*, *124*(3), 1697–1719. doi: 10.1029/2018JD029471
- 1012 Silber, I., Verlinde, J., Wang, S.-H., Bromwich, D. H., Fridlind, A. M., Cadeddu, M.,

- 1013 ... Flynn, C. J. (2019). Cloud influence on era5 and amps surface downwelling
1014 longwave radiation biases in west antarctica. *Journal of Climate*, *32*(22),
1015 7935-7949. doi: 10.1175/JCLI-D-19-0149.1
- 1016 Smith, A. J., Larson, V. E., Niu, J., Kankiewicz, J. A., & Carey, L. D. (2009).
1017 Processes that generate and deplete liquid water and snow in thin midlevel
1018 mixed-phase clouds. *Journal of Geophysical Research: Atmospheres*, *114*(D12).
1019 doi: 10.1029/2008JD011531
- 1020 Sotiropoulou, G., Sedlar, J., Forbes, R., & Tjernström, M. (2016). Summer arctic
1021 clouds in the ecmwf forecast model: an evaluation of cloud parametrization
1022 schemes. *Quarterly Journal of the Royal Meteorological Society*, *142*(694),
1023 387-400. doi: 10.1002/qj.2658
- 1024 Sotiropoulou, G., Vignon, E., Young, G., Morrison, H., O'Shea, S. J., Lachlan-Cope,
1025 T., ... Nenes, A. (2020). Secondary ice production in antarctic mixed-phase
1026 clouds: an underappreciated process in atmospheric models. *Atmos Chem Phys*
1027 *Discuss, under review*. doi: 10.5194/acp-2020-328
- 1028 Stevens, B. (2002). Entrainment in stratocumulus-topped mixed layers. *Quar-*
1029 *terly Journal of the Royal Meteorological Society*, *128*(586), 2663-2690. doi: 10
1030 .1256/qj.01.202
- 1031 Thompson, G., Field, P. R., Rasmussen, R. M., & Hall, W. D. (2008). Explicit
1032 forecasts of winter precipitation using an improved bulk microphysics scheme.
1033 part ii; implementation of a new snow parametrization. *Mon Weather Rev*,
1034 *136*(5095). (doi:10.175/2008MWR2387.1)
- 1035 Uetake, J., Hill, T. C. J., Moore, K. A., DeMott, P. J., Protat, A., & Kreidenweis,
1036 S. M. (2020). Airborne bacteria confirm the pristine nature of the southern
1037 ocean boundary layer. *Proceedings of the National Academy of Sciences*. doi:
1038 10.1073/pnas.2000134117
- 1039 Varma, V., Morgenstern, O., Field, P., Furtado, K., Williams, J., & Hyder, P.
1040 (2020). Improving the southern ocean cloud albedo biases in a general cir-
1041 culation model. *Atmospheric Chemistry and Physics*, *20*(13), 7741-7751.
1042 Retrieved from <https://www.atmos-chem-phys.net/20/7741/2020/> doi:
1043 10.5194/acp-20-7741-2020
- 1044 Vergara-Temprado, J., Miltenberger, A. K., Furtado, K., Grosvenor, D. P., Ship-
1045 way, B. J., Hill, A. A., ... Carslaw, K. S. (2018). Strong control of southern

- 1046 ocean cloud reflectivity by ice-nucleating particles. *Proceedings of the National*
 1047 *Academy of Sciences*, 115(11), 2687–2692.
- 1048 Vignon, E., Besic, N., Jullien, N., Gehring, J., & Berne, A. (2019). Microphysics of
 1049 snowfall over coastal East Antarctica simulated by Polar WRF and observed
 1050 by radar. *J Geophys Res Atmos.* doi: 10.1029/2019JD031028
- 1051 Vignon, E., Hourdin, F., Genthon, C., Van de Wiel, B. J. H., Gallée, H., Madeleine,
 1052 J.-B., & Beaumet, J. (2018). Modeling the dynamics of the atmo-
 1053 spheric boundary layer over the Antarctic Plateau with a general circu-
 1054 lation model. *Journal of Advances in Model Earth Systems*, 10, 98-125.
 1055 (10.1002/2017MS001184)
- 1056 Vignon, E., Picard, G., Durán-Alarcón, C., Alexander, S. A., Gallée, H., & Berne,
 1057 A. (2020). Gravity wave excitation during the coastal transition of an extreme
 1058 katabatic flow in antarctica. *J Atmos Sci.* doi: 10.1175/JAS-D-19-0264.1
- 1059 Vignon, E., Traullé, O., & Berne, A. (2019). On the fine vertical structure of the low
 1060 troposphere over the coastal margins of east antarctica. *Atmospheric Chem-*
 1061 *istry and Physics*, 19(7), 4659–4683. doi: 10.5194/acp-19-4659-2019
- 1062 Wille, J. D., Favier, V., Dufour, A., Gorodetskaya, I. V., Turner, J., Agosta, C., &
 1063 Codron, F. (2019). West antarctic surface melt triggered by atmospheric
 1064 rivers. *Nature Geoscience*, 12(11), 911–916.
- 1065 Wilson, T. H. (2015). *The evolution and life cycle of valley cold pools* (Doctoral
 1066 dissertation, University of California, Los Angeles). Retrieved from [http://](http://escholarship.org/uc/item/44c4k8gh)
 1067 escholarship.org/uc/item/44c4k8gh
- 1068 Young, G., Lachlan-Cope, T., O’Shea, S. J., Dearden, C., Listowski, C., Bower,
 1069 K. N., ... Gallagher, M. W. (2019). Radiative effects of secondary ice en-
 1070 hancement in coastal antarctic clouds. *Geophysical Research Letters*, 46(4),
 1071 2312-2321. doi: 10.1029/2018GL080551
- 1072 Zelinka, M. D., Myers, T. A., McCoy, D. T., Po-Chedley, S., Caldwell, P. M.,
 1073 Ceppi, P., ... Taylor, K. E. (2020). Causes of higher climate sensitivity in
 1074 cmip6 models. *Geophysical Research Letters*, 47(1), e2019GL085782. doi:
 1075 10.1029/2019GL085782
- 1076 Zhang, D., Vogelmann, A., Kollias, P., Luke, E., Yang, F., Lubin, D., & Wang, Z.
 1077 (2019). Comparison of antarctic and arctic single-layer stratiform mixed-phase
 1078 cloud properties using ground-based remote sensing measurements. *Jour-*

1079

Journal of Geophysical Research: Atmospheres, 124(17-18), 10186-10204.

doi:

1080

10.1029/2019JD030673